SCISPACE
formerly Typeset

Open access • Journal Article • DOI:10.1029/98JD02705

Gravity wave characteristics in the lower atmosphere at south pole — Source link

Matt Pfenninger, Alan Z. Liu, George C. Papen, Chester S. Gardner

Institutions: University of Illinois at Urbana–Champaign

Published on: 27 Mar 1999 - Journal of Geophysical Research (John Wiley & Sons, Ltd)

Topics: Stratosphere, Tropopause, Gravity wave, Troposphere and Convective instability

Related papers:

- A statistical study of gravity waves in the polar regions based on operational radiosonde data
- Gravity wave activity in the lower atmosphere: Seasonal and latitudinal variations
- Gravity wave dynamics and effects in the middle atmosphere
- Gravity waves in the tropical lower stratosphere: An observational study of seasonal and interannual variability
- Turbulence and stress owing to gravity wave and tidal breakdown

Share this paper:

View more about this paper here: https://typeset.io/papers/gravity-wave-characteristics-in-the-lower-atmosphere-at-18v1r3bg89

EMBRY-RIDDLE
Aeronautical University
SCHOLARLY COMMONS

Physical Sciences - Daytona Beach | College of Arts & Sciences

3-27-1999

Gravity Wave Characteristics in the Lower Atmosphere at South Pole

Matt Pfenniger

Alan Z. Liu
Embry Riddle Aeronautical University - Daytona Beach, liuz2@erau.edu

George C. Papen

Chester S. Gardner

Follow this and additional works at: https://commons.erau.edu/db-physical-sciences

 Part of the Oceanography and Atmospheric Sciences and Meteorology Commons

Scholarly Commons Citation

Pfenniger, M., Liu, A. Z., Papen, G. C., & Gardner, C. S. (1999). Gravity Wave Characteristics in the Lower Atmosphere at South Pole. *Journal of Geophysical Research, 104*(D6). Retrieved from https://commons.erau.edu/db-physical-sciences/7

This Article is brought to you for free and open access by the College of Arts & Sciences at Scholarly Commons. It has been accepted for inclusion in Physical Sciences - Daytona Beach by an authorized administrator of Scholarly Commons. For more information, please contact commons@erau.edu.

JOURNAL OF GEOPHYSICAL RESEARCH, VOL. 104, NO. D6, PAGES 5963–5984, MARCH 27, 1999

Gravity wave characteristics in the lower atmosphere at south pole

Matt Pfenninger, Alan Z. Liu, George C. Papen, and Chester S. Gardner

Department of Electrical and Computer Engineering, University of Illinois at Urbana-Champaign

Abstract. A 4-year (1993-1996) temperature and wind data set obtained from over 2000 high-resolution balloon soundings at South Pole is used to study gravity wave characteristics in the troposphere and lower stratosphere. Extensive analyses of energy density, spectra, and static stability are performed to present a comprehensive view of the gravity wave characteristics in the lower atmosphere at South Pole. Our results show that the gravity waves are ubiquitous and often fairly strong at South Pole, even though the generation mechanisms are not clear. Gravity wave characteristics are, in general, similar to those obtained at other high-latitude southern hemisphere stations. Potential energies vary between about 0.5 J/kg and 5 J/kg with season and altitude . Variations in kinetic energies are not well correlated with potential energy variations and range from 1 J/kg to 11 J/kg. We observe significant seasonal variations of the slope and magnitude of the vertical wavenumber spectrum of temperature fluctuations, especially in the stratosphere. In general, the gravity waves in the stratosphere are stronger (weaker) in austral spring (fall). Wave activity in the troposphere has little seasonal dependence. Stability analysis shows that instabilities are more likely to occur in the troposphere than in the stratosphere. The probability of wave instability is 13.7% in the troposphere and 5.4% in the stratosphere. This is due to the less stable stratification in the troposphere, where the buoyancy period averages 8.3 min compared to 4.9 min in the stratosphere. Dynamic (shear) instability is more likely to occur than convective instability (11% versus 2.6% in the troposphere and 4.7% versus 0.7% in the stratosphere), due to the prevailing strong wind shear. The instability probabilities vary seasonally with the austral winter exhibiting the highest probability of instabilities (dynamic and convective instabilities combined) in both the troposphere and stratosphere.

1. Introduction

It is now well known that gravity waves play important roles in determining the large-scale atmospheric circulation patterns above the tropopause, especially in the mesosphere and lower thermosphere. Because of their small scale, gravity waves cannot be resolved in general circulation models (GCMs), which makes it difficult to explicitly simulate their dynamical and thermal effects on the large-scale circulation. Without incorporating the gravity wave effects, GCMs do poorly in predicting the observed time mean wind and temperature structure. The major mechanism of gravity waves' influence on the mean flow is their transport of momentum and heat from the lower to the middle and upper atmosphere, therefore changing the dynamic and thermal balance of the atmosphere. To incorporate the effects of the gravity waves into GCMs, one can either increase the model resolution to resolve most important gravity waves or use some kind of parameterization to approximate the effects of gravity waves. *Hamilton* [1996] demonstrated that increasing the model resolution to resolve more waves can indeed improve the simulation of the time mean circulation. But to achieve a reasonably good result, the resolution has to be so high that the computation demand becomes prohibitive. With our current computer power, the gravity wave parameterization in GCMs is therefore crucial for the study of middle and upper atmosphere and their coupling with the lower atmosphere.

Copyright 1999 by the American Geophysical Union.

Paper number 98JD02705.
0148-0227/99/98JD02705$09.00

Several theories have been proposed to provide parameterization methods of gravity waves based on various mechanisms which, among others, include linear instability [*Dewan and Good*, 1986; *Lindzen*, 1981], nonlinear wave-wave interaction [*Weinstock*, 1990], diffusive filtering [*Gardner*, 1994], and Doppler spreading [*Hines*, 1991, 1997a, 1997b]. *Medvedev and Klaassen* [1995] also proposed a parameterization scheme that combines Weinstock's nonlinear wave-wave interaction theory and Hines' Doppler spreading theory. These theories aim at describing the evolution of wavenumber spectra and frequency spectra as the gravity waves propagate upward. Characterizing the wave spectra is the basis for most parameterizations of gravity wave drag.

For all these theories, a source spectrum has to be prescribed, which depicts the spectral shape in low-wavenumber regime. The spectrum at the high-wavenumber regime is then derived from the theories based on their assumptions of how waves interact and break as they propagate. Since most observations do not provide an adequate measure of the vertical wavenumber spectrum in the source region, the source spectrum is usually modeled using mathematically convenient forms. The most commonly used form is the "modified Desaubies" spectrum proposed by *VanZandt and Fritts* [1989]. This form is used by *Fritts and VanZandt* [1993] and *Fritts and Lu* [1993] to study the gravity wave energy and momentum fluxes and their parameterization. Recently, several observational studies have emerged which address in detail the characteristics of gravity waves in the lower atmosphere (*Allen and Vincent*, [1995], AV95 hereafter; *Nastrom et al.*, [1997], NVW97 hereafter; among others). While focused on the high wavenumber spectrum, these studies also indirectly addressed the shape of the source spectrum. In this work, we characterize the gravity wave climatology in the lower atmosphere over South

Pole using temperature and wind measurements obtained from over 2000 balloon soundings launched between January 1, 1993 and December 31, 1996. The results would expand the spatial coverage of gravity wave studies in the lower atmosphere, which remain sparse, with most experiments concentrated at low-latitude and midlatitude sites. With the relatively high altitude reached by balloon soundings, this data set enables us to extend the gravity wave spectrum to the lower wavenumber regime, which is helpful for determining the shape of the gravity wave source spectrum.

Several factors combine to make the south pole a unique environment to study gravity waves. In northern hemisphere midlatitudes, gravity waves are constantly generated by orographic forcing and storm activities. The characteristics of these waves in the lower atmosphere are largely determined by the sources. The relatively featureless Antarctic plateau provides few obstructions which could generate waves by orographic forcing, a mechanism which tends to generate strong monochromatic waves. After sunset in March, convection is expected to quickly subside, leaving the atmosphere in relatively quiet equilibrium. Due to the extremely cold and dry conditions, frontal activity is minimal throughout the year. Study of gravity waves at South Pole could therefore provide a unique insight to the gravity wave characteristics in the absence of the two major wave generation mechanisms. Even with minimal orographic forcing and frontal activities, gravity waves can still be present at South Pole, from waves propagating from other regions as well as generated by instabilities due to strong wind shear. The study of gravity waves at South Pole not only extends of our understandings of their characteristics to higher latitudes, but also is important for the understanding of the polar circulation, which has features distinctive from those in midlatitudes and tropics. Some of these features cannot be explained without taking into account of the gravity waves. For example, the thermal structure of the polar stratosphere may be driven by gravity waves [*Hitchman et al.*, 1989].

This paper is organized as follows. In section 2, we describe the instrumentation and data acquisition at South Pole. Section 3 presents the method we used to determine the separation between the wave perturbations and the background from the raw wind and temperature data. It is followed by a short description of the mean atmospheric environment in section 4. Section 5 presents the analysis of energy density distribution of gravity waves. Section 6 is the analyses of vertical wavenumber spectra of wind and temperature perturbations. In section 7, we examine the propagation direction of gravity waves. The stability of gravity waves is presented in section 8. The results are then discussed and summarized in section 9.

2. Radiosonde Measurements

The meteorology office at Amundsen-Scott South Pole Station conducts daily, high-resolution radiosonde measurements as part of the U.S. Antarctic Research Program. For several years, launches have occurred daily at 0800 (UT) with additional launches at 2000 (UT) during the austral summer (mid-October through mid-February) in support of airlift operations to South Pole Station. Conveniently, these data have been archived in raw form since January 1993, providing a unique opportunity for studying lower atmospheric gravity wave activity over the Antarctic plateau.

Throughout this period, balloon payloads have been the Atmospheric Instrumentation Research (AIR) model IS-4A-1860 radiosondes which concurrently sample pressure p (0.01 mbar resolution, 0.1 mbar accuracy), temperature T (0.01°C resolution, 0.5°C accuracy), and relative humidity (0.01% resolution, 3% accuracy) every 2 to 3 s during the balloon's ascent. On-the-fly calculations by the radiosonde system determine the geopotential for each measurement. In our processing, we compute the potential temperature for each sample using

$$\theta = T\left(\frac{p_s}{p}\right)^{\kappa}, \tag{1}$$

where $p_s = 1000$ hpa and $\kappa \approx 2/7$.

The usefulness of the radiosondes is enhanced by a radiotheodolite system (0.025° resolution, 0.05° accuracy, azimuth and elevation) which tracks the sonde's flight to determine its speed and direction. Although the vertical component of this motion is due primarily to the ascent of the balloon, horizontal motion is caused by horizontal winds which we represent on a Cartesian coordinate system with v component along grid north (the prime meridian) and u component along grid east (90° east of the prime meridian). A single value for the uncertainty in wind velocity is impossible to determine, as it depends nonlinearly on the altitude and elevation angle of the radiosonde, and the time interval between successive measurements. To first order, we approximate the wind velocity uncertainty using representative values for the uncertainties in these parameters. If the radiotheodolite is pointed 15° from vertical and locates the sonde once every 2 s (when the sonde transmits its sampled values), wind resolution at 20 km is approximately 5 m/s.

Almost every flight is limited by catastrophic balloon failure. Therefore the maximum measurement altitude varies from launch to launch (see Figure 1). Summer soundings typically reach altitudes of 30 to 35 km, but coverage is reduced in winter since balloon elasticity is severely reduced by the extremely cold lower stratosphere. To partially compensate for this effect, twice each week in the winter 7000 in.^{3} balloons are substituted for the usual 600 in.^{3} balloons, extending the maximum altitude from ~14 km to ~25 km. The 4-year average maximum altitudes attained in each month are shown in Table 1.

Several studies have determined that typical ascent rates of 5 to 10 m/s are sufficiently rapid to sample the vertical wavenumber spectrum without significant distortion from either the finite sampling rate or the horizontal displacement of the sonde during flight [Lalas and Einaudi, 1980; Sidi et al., 1988; Gardner and Gardner, 1993]. In addition, AV95 have stressed the importance of compensating the temperature spectra for temporal lag in their Vaisala temperature sensor. We have not performed this compensation because, as will be shown in section 6, our temperature spectra do not show the high wavenumber roll-off characteristic of this lag, suggesting that temporal lag in the AIR sonde's temperature sensor is negligible.

Our analyses of the vertical wavenumber spectra of wind velocity measurements (also in section 6) differ considerably from the canonical model spectrum common to the prominent theories of gravity wave propagation and dissipation [*VanZandt and Fritts*, 1989; *Fritts and VanZandt*, 1993]. Although the low-vertical-wavenumber content of the wind velocity measurement is believed to be accurate, we suspect that the proprietary variable-width filtering mechanism in the radiotheodolite tracking system has compromised the accuracy of the high vertical wavenumber content of the wind velocity measurements. Even though the short vertical scale wind measurements are distorted by the data processing algorithms, we include analyses of winds here for completeness and to stress the important science that can be achieved by combining the wind and temperature data.

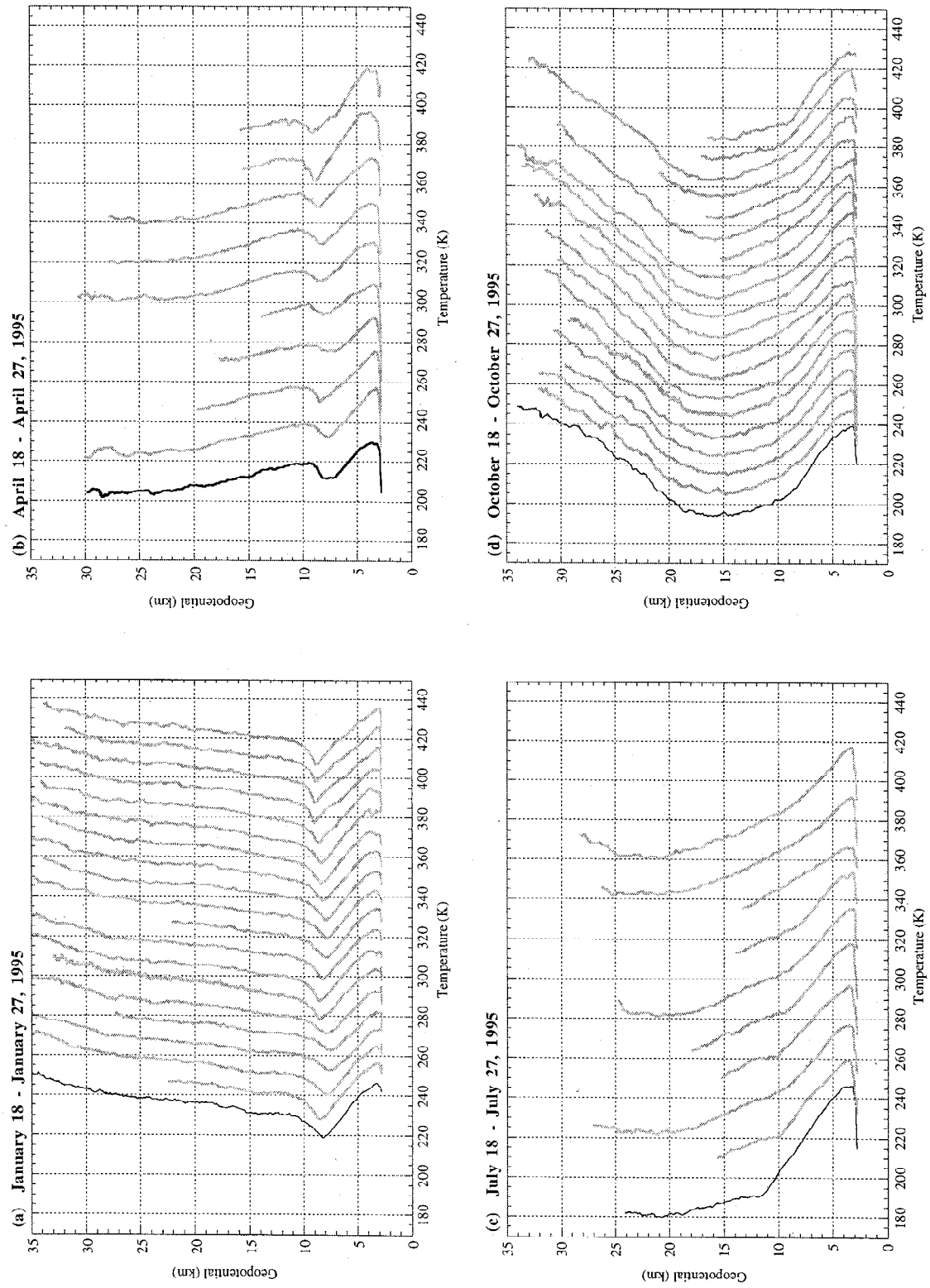

Figure 1. Representative temperature profiles at South Pole for (a) January, (b) April, (c) July, and (d) October, 1995. Successive profiles are displaced by 10 K in Figures 1a and 1d and by 20 K in Figures 1b and 1c.

Table 1. Monthly Mean Maximum Balloon Altitude (km), 1993-1996

Month	Altitude, km
January	30.7
February	29.9
March	29.8
April	22.3
May	20.0
June	18.6
July	17.5
August	17.8
September	18.4
October	24.0
November	28.2
December	29.6

3. Separating Wave Perturbations From Synoptic Structure

Separating fluctuations caused by gravity wave activity from the non-gravity-wave fluctuations is probably the most difficult task in our study of the lower atmosphere. Fundamentally, we assume that each measured profile of temperatures and winds (T, u, and v) is a simple superposition of gravity wave perturbations (T', u', and v') on a background structure (T_0, u_0, and v_0). Here, the background includes all non-gravity-wave fluctuations such as seasonal variations and synoptic disturbances. Our goal is to isolate the two components given the measured profile.

Other studies have used polynomials of varying orders to represent the synoptic structure within limited regions of the atmosphere (AV95, NVW97). Typically, one polynomial is used in the troposphere and another is used in the stratosphere. Due to the inflexibility of polynomials of moderate order over large spans, these techniques are fundamentally limited to regions of moderate extent (less than 10 km) and small synoptic variability. Since a fundamental goal of this work was to extend our estimates of gravity wave spectra to longer vertical wavelengths, we require a modeling technique which provides reasonable estimates of the background structure over extended height regions. Our solution is a two-step process. First, the raw data are smoothed temporally to extract a majority of the background structure. Then, low-order polynomials are fit to the difference between the measured and smoothed profiles. The background profile is then defined as the sum of the smoothed profile plus the polynomial fit.

We have selected a two-dimensional Hanning window

$$w(z,t)=\begin{cases}\frac{1}{4}\left[1+\cos\left(\frac{\pi z}{\alpha}\right)\right]\left[1+\cos\left(\frac{\pi t}{\beta}\right)\right] & -\alpha\le z\le\alpha \\ & -\beta\le t\le\beta \\ 0 & \text{elsewhere}\end{cases} \quad (2)$$

for the smoothing kernel because it is easy to implement and it minimizes spectral energy leakage from high frequencies (and wavenumbers). The filter is applied in the time-space domain as a weighted average centered at each sample. For example, the smoothed value of temperature at location (z, t) is

$$T_s(z,t)=\frac{\sum_{i,j} w(z-z_i,t-t_j)T(z_i,t_j)}{\sum_{i,j} w(z-z_i,t-t_j)}$$

$$\forall_{i,j}:|z-z_i|<\alpha \text{ and } |t-t_j|<\beta. \quad (3)$$

This formula is applied once for each sample in the data set, producing estimates of the background structure coincident with the original measurements.

Because we have only one or two launches each day, portions of the (m,ω) spectrum which contain gravity waves are aliased down into lower frequencies as described by the Nyquist sampling criterion. When we apply the spatio temporal filter to the under sampled data set, we inadvertently include in the passband those portions of the gravity wave spectrum which have been mapped to lower frequencies by aliasing. For a sampling rate of $(12\text{ hours})^{-1}$, waves with frequencies near each integer multiple of $2\pi/(12\text{ hours})$ are included in the smoothed profile. By maximizing α and β, we narrow the spectrum of our window, minimizing aliasing distortion.

Maximizing α and β also improves our robustness to signal dropouts. Dropout conditions are most pronounced in the winter stratosphere, where only one or two launches each week attain altitudes above 15 km. Increasing α allows the filter to span multiple profiles to improve our estimate of the background. However, as α and β increase, the filter looses its ability to model smaller scale synoptic structures. So we are left with a trade-off between robustness and flexibility.

After considerable experimentation, we settled on a temporal half-width α of 14 days (2 weeks) and spatial half-width β of 2 km (RMS widths: 5 days × 720 m). This particular choice of widths successfully represented a majority of the synoptic structure throughout all 4 years. However, due to the large temporal window required to minimize aliased gravity wave energy loss, the smoothing was often insufficiently flexible in modeling the large spatial scale, profile-to-profile variations of the data. A second step is needed to compensate for short-term temporal variations that has a minimal effect on the vertical spectra.

Since most of the synoptic variations have been accounted for by the smoothing, low-order polynomial fits to the residual profiles are sufficient to model the remaining synoptic structure. We use a second-order polynomial in the troposphere (from 4 km to 8 km) and a third order polynomial in the stratosphere (10 km to the end of the profile). These low-order polynomials do not significantly alter the m-spectrum of gravity waves, yet they do remove portions of the background structure which could not be described by the smoothed data alone.

The computation of wind and temperature perturbations is illustrated in Figure 2. In this figure, the gray curve is the raw radiosonde profile. The dashed curve is the background profile computed by smoothing the raw data using the 2-D Hanning window. Notice that the smoothed data can exhibit large biases, especially in the two components of wind. The solid line is the final background structure after the low-order polynomial fits have been added to the smoothed profile. The polynomial fit compensates for profile-to-profile variations that cannot be represented by the smoothed data alone.

4. Background Environment

The background environment can have a striking influence on the propagation and dissipation of gravity waves. It is the temperature structure (along with the pressure gradient) which establishes the stratified conditions necessary for buoyancy oscillations to occur [*Holton*, 1992]. Changes in the temperature structure directly affect the natural period of oscillation, modifying the dissipation characteristics of propagating waves. Horizontal winds can Doppler shift the vertical wavelengths of propagating waves. In regions of extreme horizontal wind shear, this can lead to se-

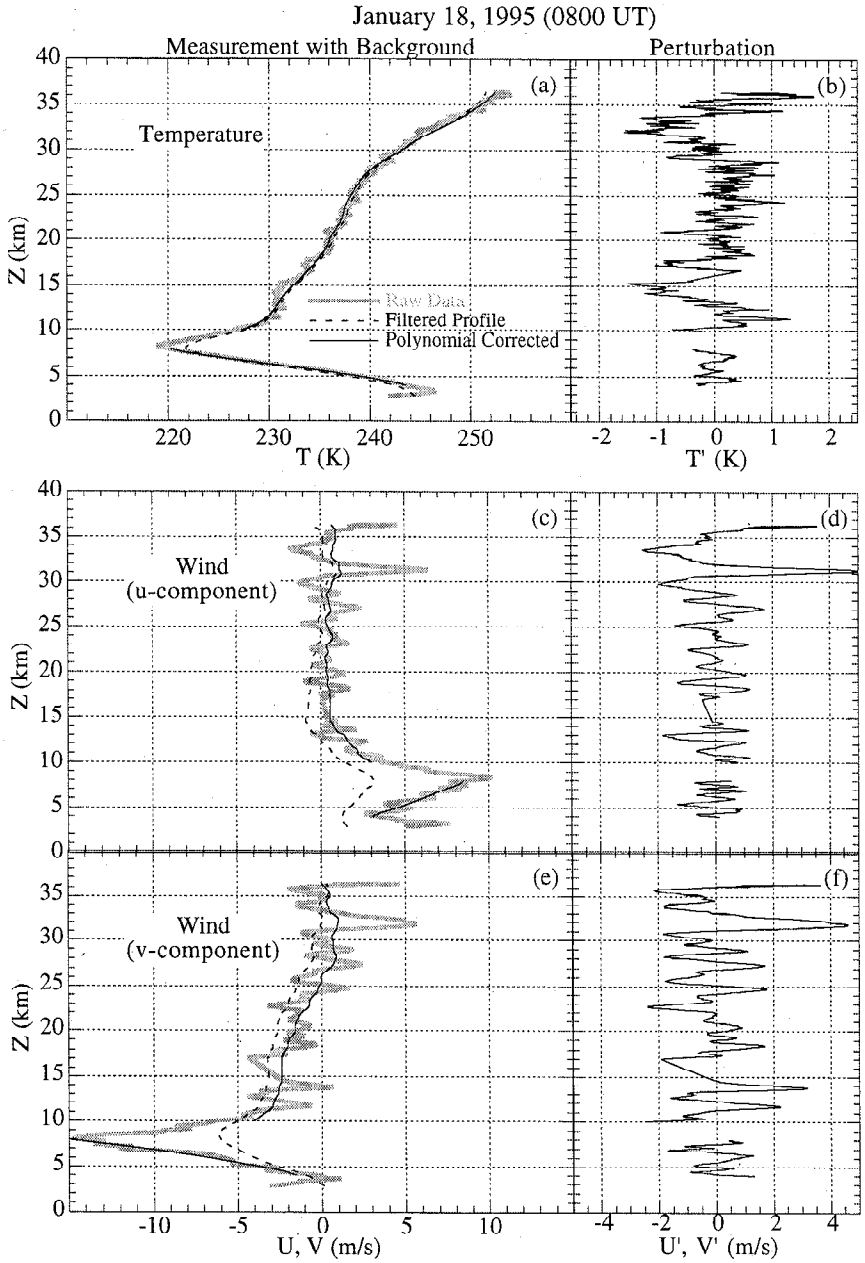

Figure 2. Sample (a) temperature and (c and e) horizontal wind profiles, displaying the original data (gray line), the profiles determined from filtering the raw data (dashed line), and the final background profiles after polynomial corrections have been added to the filtered profiles. Differences between the raw profiles and the corrected background are caused by gravity waves (Figure 2b, 2d, and 2f).

lective filtering as waves are Doppler shifted to frequencies which cannot propagate through the shear [*Eckermann*, 1995].

A contour plot of the mean background temperatures over South Pole is shown in Plate 1a. As expected for a high latitude site, the tropopause is quite low (between 8 and 9 km), only 5 km above the surface. Tropospheric temperatures remain relatively constant throughout the year, changing by no more than 10 K at any given altitude above the boundary layer (lowest 300 m). Stratospheric temperatures drop dramatically after sunset in late March, reaching a minimum of about 180 K near 20 km in late July. After sunrise in mid-September, midstratospheric temperatures increase quickly to a maximum of about 260 K at 35 km in late October, then decrease slightly in late November. The temperature increase slowly progresses downward through the lower stratosphere, resulting in a strong vertical temperature gradient from mid-September through the end of November. As seen in the mean wind plots of Plates 1b and 1c, coincident with this strong temperature increase is an increase in the mean winds.

The static stability of a region of atmosphere can be described by the mean buoyancy frequency N^2, determined from

$$N_0^2 = g\frac{\partial \ln \overline{\theta}}{\partial z}, \tag{4}$$

where $g = 9.8\ \mathrm{m/s^2}$ and $\overline{\theta}$ is the mean potential temperature. The derivative in (4) is approximated by finite difference of $\overline{\theta}$, which is binned onto a 1 week × 500 m grid.

The resulting mean buoyancy frequency, displayed as buoyancy period ($2\pi/N_0$) is shown in Plate 2, where shorter buoyancy period implies greater stability. The buoyancy period typically lies between 5 and 9 min in the troposphere and between 3 and 6 min in the lower stratosphere. Notice that the troposphere is least stable in the austral winter due to large negative vertical temperature gradient associated with the cool stratosphere. An annual downward phase progression in buoyancy period is clearly evident in the stratosphere. This phase progression is related to the annual cycle of solar heating and radiative cooling observed in the mean temperature structure (Plate 1a).

5. Energy Density

In this section, we determine the distribution of wave energies with altitude throughout the year. The distributions of potential and kinetic energies contained in the wave field are computed directly from the temperature and wind perturbations. The potential energy density

$$PE = \frac{g^2 \overline{(T'/T_0)^2}}{2N_0^2}, \tag{5}$$

is computed from the values of mean buoyancy frequency N_0 of Plate 2 and the mean temperature T_0 of Plate 1. The relative temperature variance $\overline{(T'/T_0)^2}$ is resolved on a 1 week × 500 m grid.

Kinetic energy density is defined as

$$KE = \frac{1}{2}\left(\overline{u'^2} + \overline{v'^2}\right), \tag{6}$$

where u'^2 and v'^2 are the mean square wind perturbations resolved on the same 1 week × 500 m grid as the relative temperature perturbations above. In our initial analyses of kinetic energy densities, we noticed that extremely large values in a few (< 1%) wind velocity measurements were dominating the mean kinetic energy. These samples almost always occurred in regions of high wind measurement uncertainty where elevation angles were less than 30° above the horizon. To reduce the influence of this small number of readings, wind perturbations which exceed the hard limit of 10 m/s have been omitted from the kinetic energy calculations.

Overall, the potential energy density (Plate 3a) lies between 1 and 1.5 J/kg, with the largest values (2 - 3 J/kg) occurring in the middle stratosphere during austral spring, exactly coincident with the strong temperature gradient shown in Plate 1a. The magnitudes of these potential energies agree reasonably well with the AV95 analysis of balloons launched from Davis Station (68.6°S, 78.0°E). Although the winter stratosphere has a slight increase in potential energy, most of the year is relatively quiet. The occasional local increases can usually be attributed to single events which are strong enough to affect the 4 year mean.

Kinetic energy density (shown in Plate 3b) is almost always larger than potential energy density by at least a factor of 4. We see two large-scale kinetic energy maxima. The first is located in the region of stratospheric heating in austral spring, coincident with the increased potential energy density. The second and more enduring maximum lasts throughout the winter stratosphere. Since we see very little increase in kinetic energy density below the tropopause, it seems likely that these waves are generated within the tropopause. We also notice that the large kinetic energy maximum does not correspond to an increase in potential energy.

Overall, the total energy density (shown in Plate 3c) is generally greater than the values determined in AV95 above Davis by roughly a factor of 2. In the lower stratosphere, the total energy density above Davis is maximum from midsummer through late fall. Total energy density in the lower stratosphere above South Pole is largest in mid-winter due to the strong increase in kinetic energy. Middle to upper stratospheric energy densities show a marked increase in the summer, with the energy increase at South Pole leading that at Davis by about 2 months. Our processing method excludes measurements at the tropopause, so we cannot confirm the large energy maximum that AV95 show at the summer tropopause above Davis.

For further comparison with AV95, we have determined the relative temperature variance $\overline{(T'/T_0)^2}$ in the altitude region they define as the stratosphere (16 - 23 km). As with AV95, the error bars represent the 95% confidence intervals. As seen in Figure 3, our data follow the latitudinal trends suggested by AV95, showing decreasing relative temperature variance with increasing southern latitude in the spring and fall data. However, we do observe slightly stronger wave activity over South Pole than they observed over Davis in both winter and summer seasons.

6. Vertical Wavenumber Spectra of Temperature and Wind

6.1. Method

The vertical wavenumber spectrum characterizes the distribution of gravity wave energy as a function of vertical wavelength. Various mechanisms have been proposed to explain the observed spectra [e.g., *Dewan and Good*, 1986; *Lindzen*, 1981; *Weinstock*, 1990; *Gardner*, 1994; *Hines*, 1991, 1997a, b; *Medvedev and Klaassen*, 1995], which generally follow a power law functional form in the so-called wave saturation region ($m > m_*$, or equivalently, wavelengths shorter than a few kilometers). It is generally agreed that in this region, the spectrum is approximately proportional to N^2/m^3. The spectrum for longer wavelength waves is much less known. The spectrum in this region is dominated by gravity wave source spectrum and is often assumed in theoretical studies [e.g., *Gardner*, 1994; *Fritts and VanZandt*, 1993]. Observational studies are limited by the vertical extent of the raw data which are often limited to only a few kilometers [AV95; NVW97; *de la Torre et al.*, 1997]. Such short height intervals preclude analyses of the spectrum in the low wavenumber region where source characteristics dominate. The South Pole radiosonde data have a relatively large vertical extent, regularly reaching above 30 km in the austral summer, enabling us to estimate the vertical wavenumber spectrum with wavelengths as long as 15 km in the lower stratosphere.

The spectral analysis techniques used in this paper differ somewhat from those used by AV95 and NVW97. Although we also perform separate analyzes in the troposphere (4 - 8 km) and the stratosphere (10 km and above), we have chosen not to artificially limit the vertical extent of our stratospheric measurement region in order to extend our measured spectra further into the low wavenumber region. Also, we compute spectra of absolute temperature perturbations instead of normalized temperature perturbations. The spectra we obtain can be compared with those based on normalized temperature perturbations by simply dividing our spectral magnitudes by the square of the mean temperature $\overline{T_0}^2$. In the spectral plots shown in this section, the axis of the spectral magnitudes are labeled with both their actual values

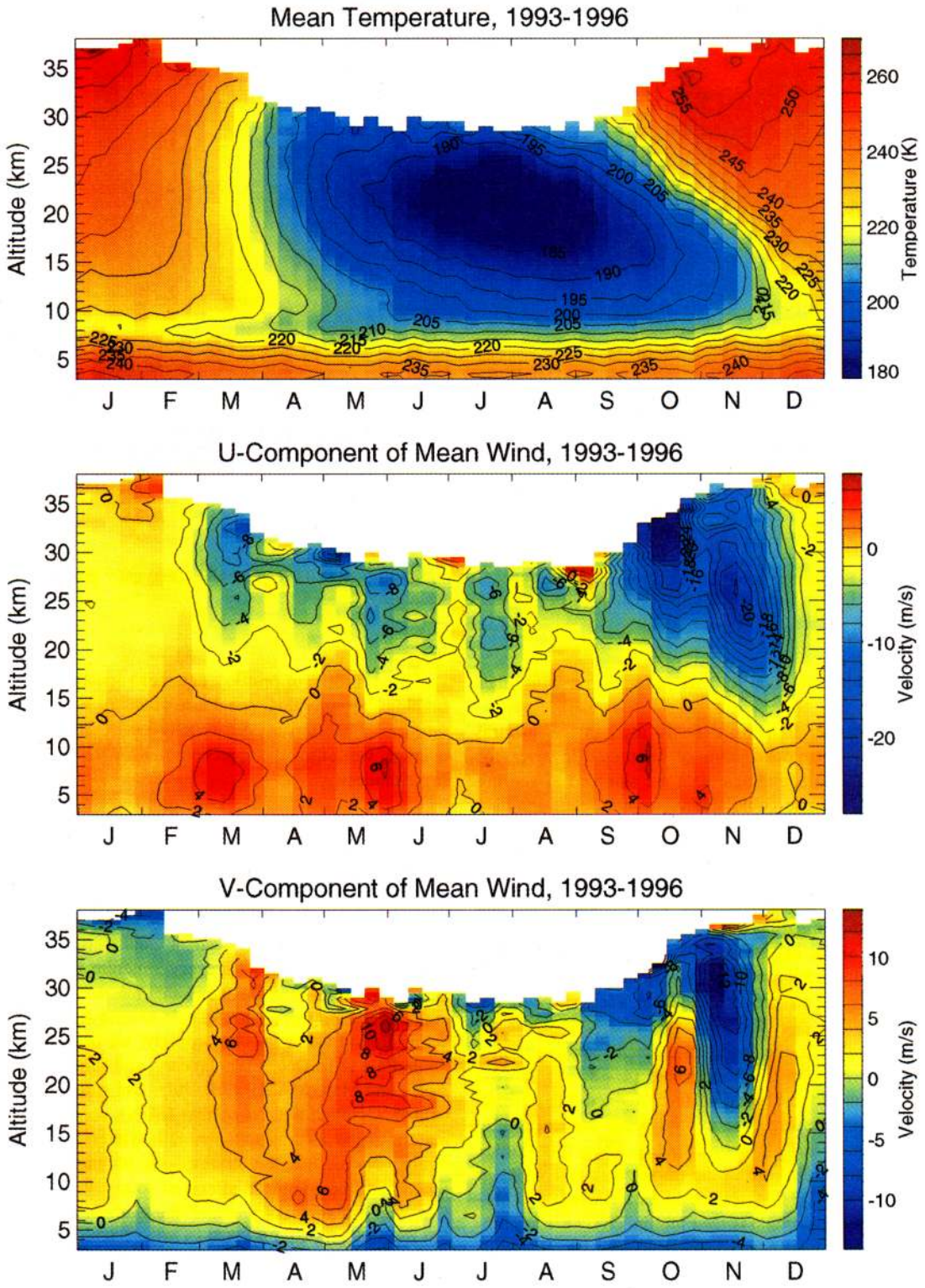

Plate 1. (a) Mean temperature and (b and c) both components of the mean horizontal wind over South Pole derived from radiosonde measurements. Raw data have been deresolved by binning to a regular 1 week × 500 m grid. A 3 week × 1.5 km Hanning filter has been applied to Plate 1b and 1c to improve readability.

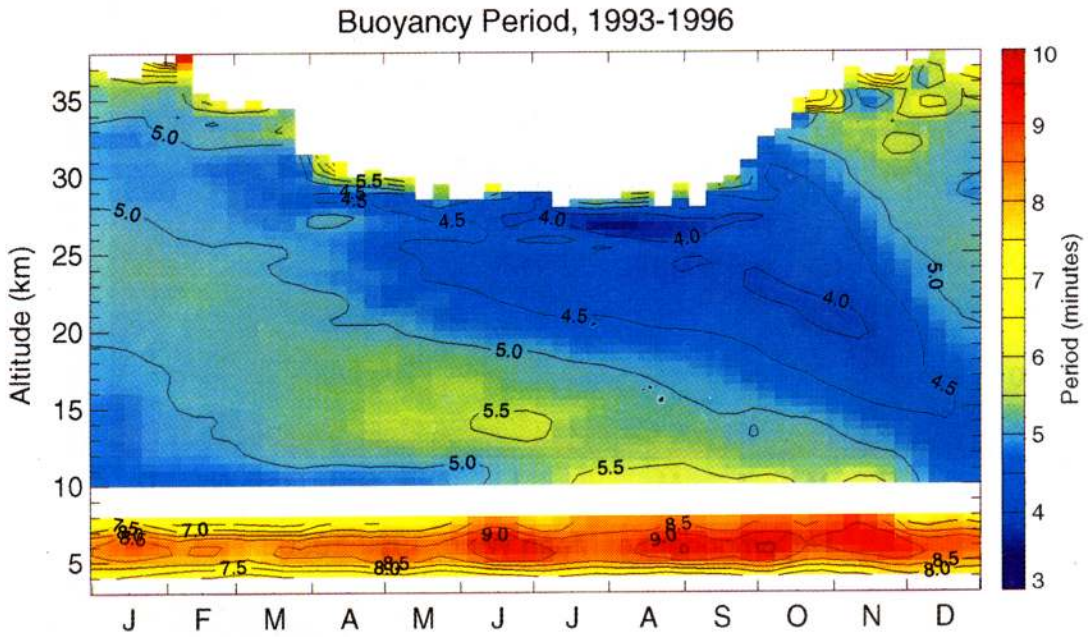

Plate 2. Buoyancy period over South Pole Station. Greater stability results in a smaller buoyancy period. A 3 week × 1.5 km Hanning filter has been applied to improve readability.

and the values scaled by $(200\ \mathrm{K})^{-2}$ for comparison with other studies.

The discrete Fourier transform (DFT) used in the spectral analysis requires uniform distribution of samples. However, for the South Pole balloon soundings, data are sampled at varying vertical intervals. We use cubic splines to interpolate the data onto a uniform grid with interval $\delta z = 20$ m. More than 95% of the raw data have sufficient resolution for correct interpolation. The remaining few percent of samples have dropouts which can be as large as a few kilometers. To prevent these few bad soundings from contaminating the time mean spectra, we compare the variance of the interpolated data to the variance of the original data and discard those soundings whose variances differ by more than 10%. This process excluded about 10% of the original soundings.

After the interpolation, the spectrum of each sounding profile is calculated separately in the troposphere (4 - 8 km) and the stratosphere (10 km to the highest altitude attained this profile). To minimize sidelobe leakage, we multiply each vertical profile by a Hanning window $w = \frac{1}{2}[1 - \cos(2\pi z / L)]$, where L is altitude range of each profile ($L = 4$ km in the troposphere and varies in the stratosphere). The DFT is performed on the windowed profile, and the spectral magnitude is then multiplied by 8/3 to compensate for the loss in total power associated with Hanning windowing.

Prewhitening is another method often used to reduce sidelobe leakage. It is achieved by performing the DFT on the vertical derivative of the data and then dividing the spectrum by m^2. For our data, there is no noticeable difference between the spectra obtained by prewhitening then applying a Hanning window and the spectra obtained by only applying a Hanning window. In all the spectral analysis presented in this paper, only the Hanning window method is used.

Since the profiles in the stratosphere have different lengths, the wavenumbers at which the spectral magnitudes are calculated vary from profile to profile. The mean spectra are determined by binning the individual spectra to standard wavenumbers, with a uniform resolution of $\Delta m = 2\pi/(40\ \mathrm{m})$. When calculating the average, we follow the approach of NVW97, and average spectra logarithmically,

$$\log F_{avg}(m) = \frac{1}{N}\sum_{i=1}^{N} \log F_i(m). \qquad (7)$$

This approach is different from that of AV95, who employ a simple arithmetic average.

Since there are large variations in the background temperature structure throughout the year at South Pole, we calculate the mean spectra separately for every 3 months to examine their seasonal variation. Plate 1a shows that the stratosphere experiences a fast transition from warm to cold around April and from cold to warm around October. Accordingly, we define four seasons at South Pole to be December, January, and February (DJF); March, April, and May (MAM); June, July, and August (JJA); and September, October, and November (SON), corresponding approximately to the austral summer, fall, winter, and spring, respectively. Notice that the stratospheric temperature variation is a function of the combined affects of solar UV heating (O_3 absorption) and radiative cooling and does not closely follow the Sun. For example, the Sun reaches its largest zenith angle around June 21, while the stratosphere temperature does not reach minimum until 1 month later. We believe that the seasonal definition according to the temperature change is more relevant to the spectral analysis than that according to the zenith angle of the incoming solar radiation.

6.2. Seasonal Mean Spectra

The mean temperature spectra are shown in Plate 4. In the troposphere, the temperature spectrum closely follows a power law form for the middle range of m, where the magnitudes are similar for all seasons. At the high wavenumber end, magnitudes

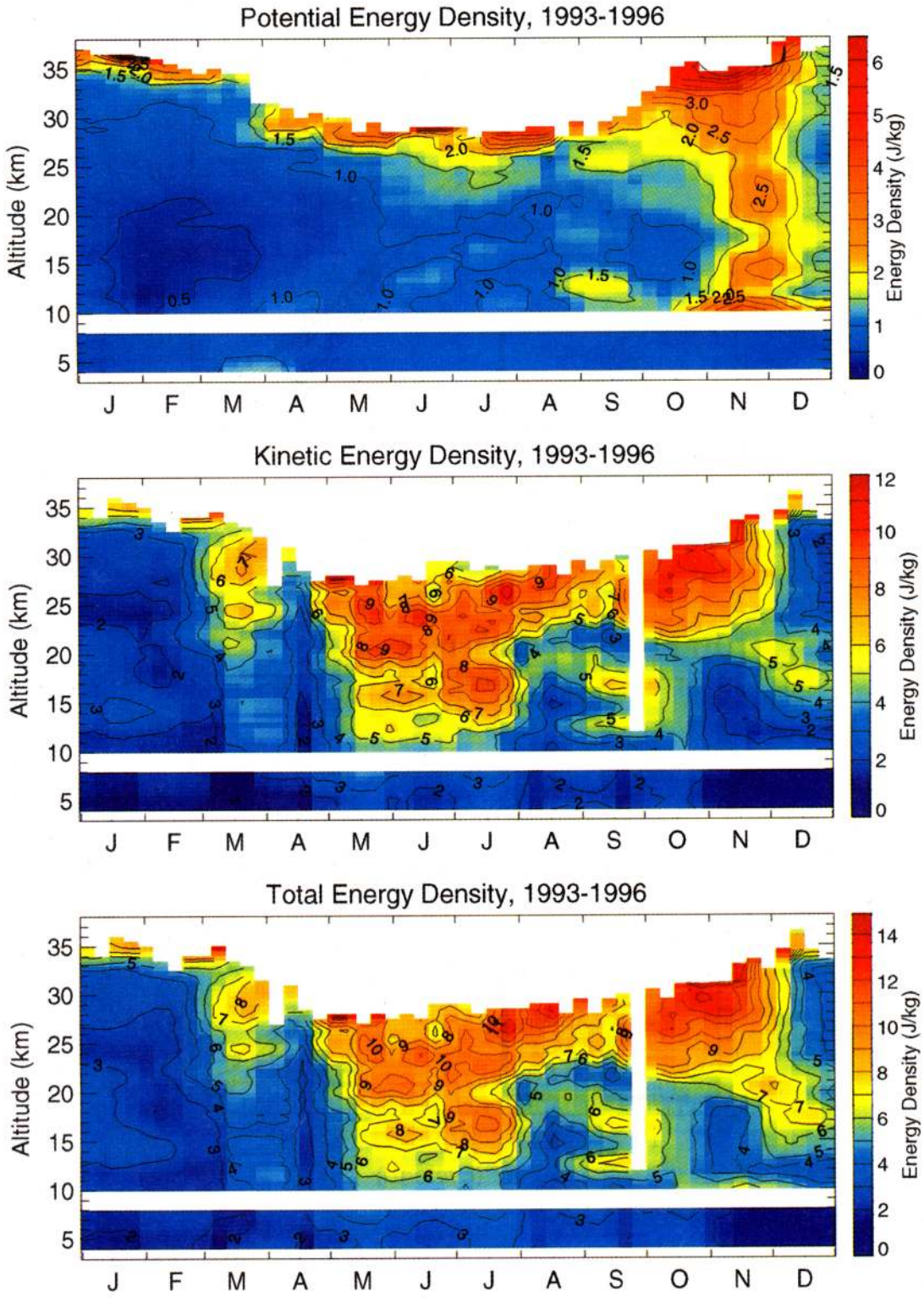

Plate 3. (a) Potential, (b) kinetic, and (c) total energy density over South Pole deresolved to a 1 week × 500 m grid. Data has been smoothed by a 5 week × 2.5 km Hanning filter to improve readability.

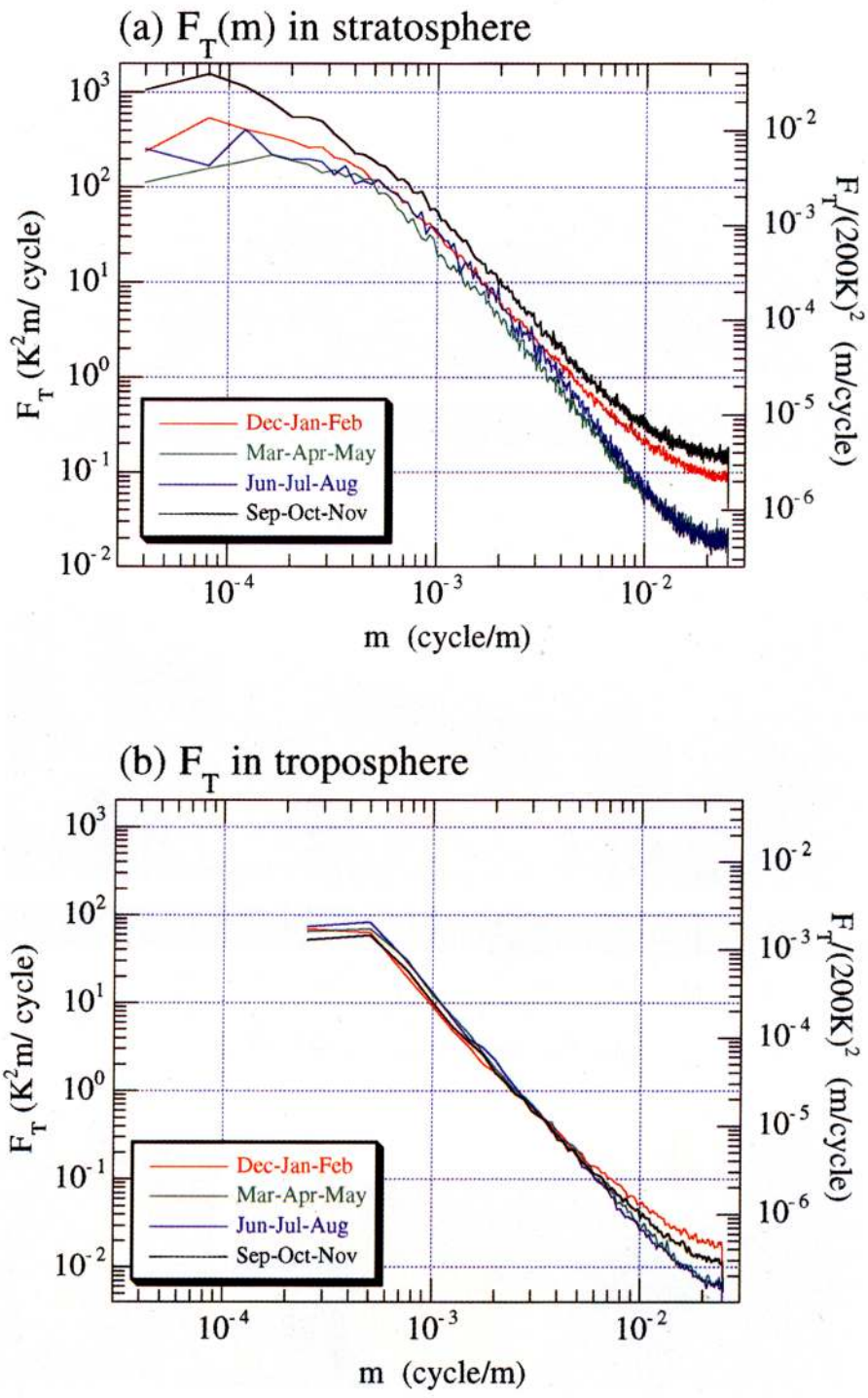

Plate 4. Seasonal mean temperature spectra in the stratosphere(a) and (b) troposphere.

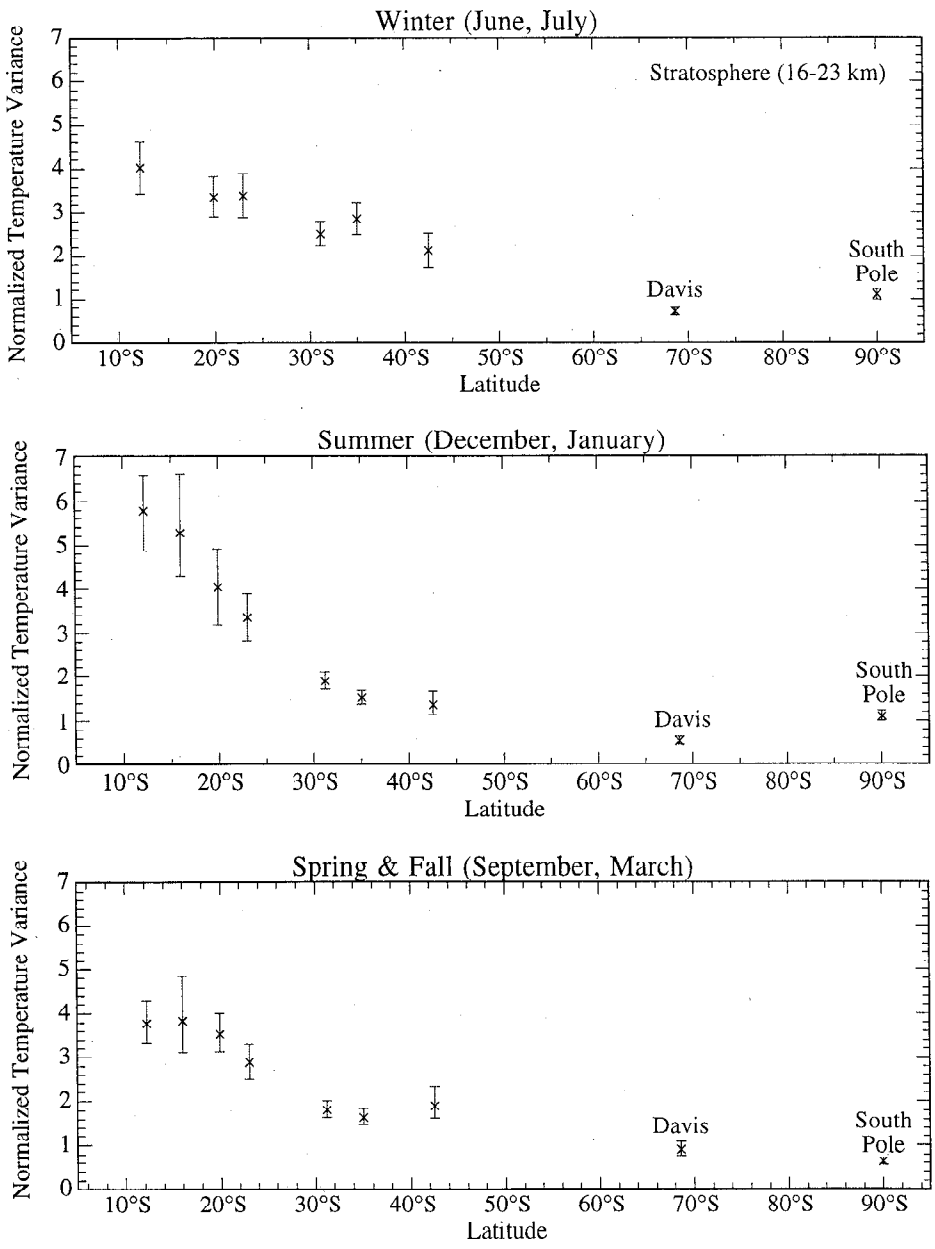

Figure 3. Variation of normalized temperature variance as a function of latitude within the lower stratosphere (16 - 23 km at Davis and South Pole, 17 - 24 km in most others). Variance at South Pole is from this work. All other values have been duplicated with permission from AV95.

are largest in the austral summer, possibly related to small-scale disturbances generated by solar heating in the boundary layer.

The temperature spectra in the stratosphere show a large variation among the seasons. At the high wavenumber end, the spectra are nearly 1 order of magnitude stronger in SON and DJF than in MAM and JJA. Because of the large vertical extent of the stratospheric soundings, the spectra can be extended to much smaller wavenumbers than in most other studies. This enables us to get a better estimate of the spectra below $m_* \approx 2\pi/(2\text{ km})$, the wavenumber that separates source region and the saturation region [*Fritts and VanZandt,* 1993; *Gardner,* 1994]. The typical value of m_* is $2\pi/(2\text{ km})$ near the tropopause [*Fritts and VanZandt,* 1993]. In Plate 4, we can see that the spectral slope in the stratosphere is negative for $m > 2\pi/(1.6\text{ km})$, and positive for $m < 2\pi/(12.5\text{ km})$. There is a transition region in between where the slope is small negative. One significant aspect of these spectra is that they do not peak at $m_* \approx 2\pi/(2\text{ km})$ as virtually all of the spectral models assume. This issue is addressed in detail by J. S. Qian and C. Gardner (Modeling the spectra of gravity perturbations in the atmosphere: Influence of the lower atmospheric sources, internal EOSL report) and appears to be related to the spectra of the wave sources.

Wind spectra are shown in Plate 5. The spectra have much steeper slopes at the high wavenumber range compared to the temperature spectra. Wind spectra reach peak values at around $2\pi/(2\text{ km})$ in the troposphere and at around $2\pi/(10\text{ km})$ in the

stratosphere. For weak gravity wave fluctuations in an isothermal atmosphere, the horizontal wind and temperature spectra are approximately proportional to each other for medium frequency waves ($f << \omega << N$). The constant of proportionality is given by the polarization relations

$$\left(\frac{g}{NT}\right)^2 F_T \approx F_u + F_v. \quad (8)$$

Figure 4 shows the 4-year averaged wind spectra together with the temperature spectra scaled by (8), using the 4-year mean temperature and mean buoyancy frequency. Notice that the wind spectra have a much steeper slope than the temperature spectra. We suspect that this is a result of the proprietary filtering process employed during the data acquisition which excessively attenuates the high vertical wavenumber components of the spectrum.

6.3. Slope and Magnitude of the Temperature Spectra

In the saturation region, the temperature spectra generally follow a power law form. The slope and magnitude of the spectra in the power law regime are two main parameters describing the characteristics of the spectrum in this region. We calculated these two parameters for all soundings to examine the variations between troposphere and stratosphere and their variation with different seasons. Spectral slope is determined by computing the least squares linear fit over the range $2\pi/(200\,\mathrm{m})$ to $2\pi/(1000\,\mathrm{m})$. Before the fit, a white noise floor is subtracted from each spectrum. The noise floor is determined by averaging the spectrum over wavelengths shorter than 50 m.

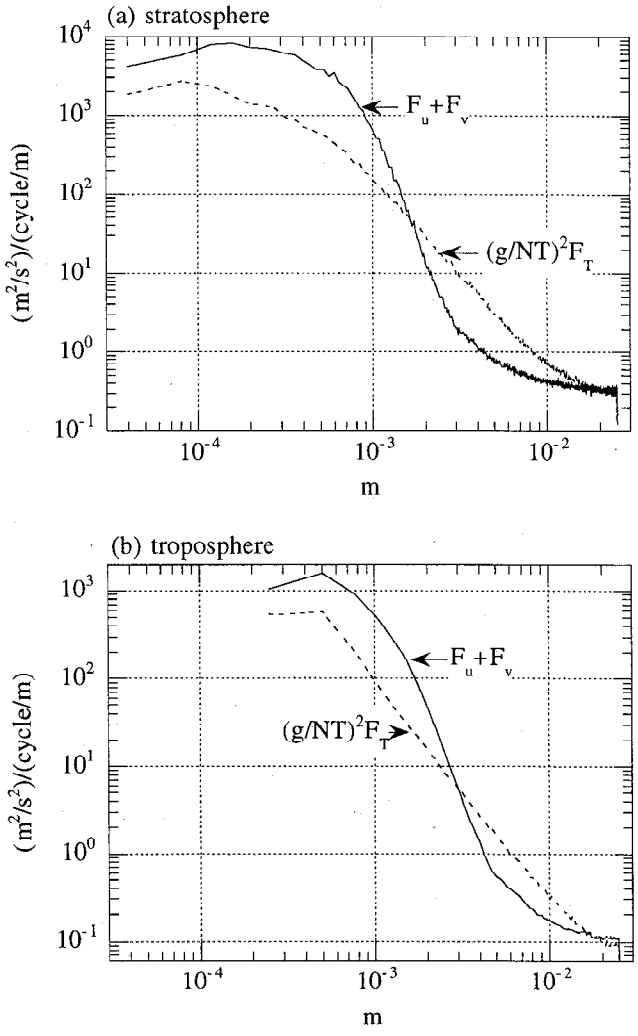

Figure 4. Comparison of 4-year average temperature and wind spectra. Temperature spectra are scaled for comparison with the wind spectra using T=225 K and N=0.015 s^{-1} in the troposphere; and T=216 K and N=0.021 s^{-1} in the stratosphere.

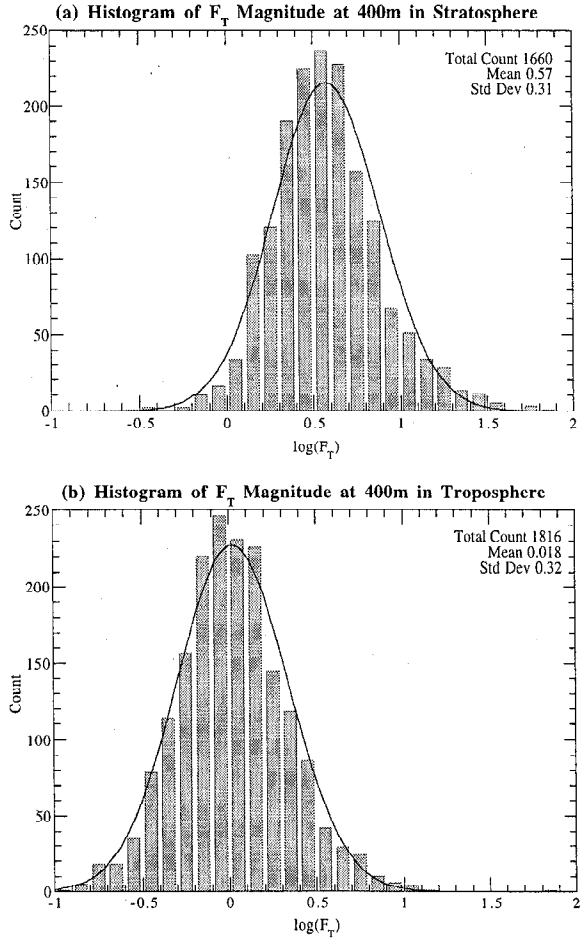

Figure 5. Histogram of the spectral magnitudes of temperature variations evaluated at $m = 2\pi/(400\ \mathrm{m})$ and their best fit Gaussian distribution in the stratosphere (a) and troposphere (b).

Histograms of the log magnitude at $m = 2\pi/(400\ \mathrm{m})$ and the slope of the power law fit are plotted in Figures 5 and 6. The histograms of log magnitude are approximately Gaussian in both the stratosphere and the troposphere, but the mean values differ (0.57 in the stratosphere, and 0.018 in the troposphere). The mean magnitude in the stratosphere is about 3~4 times as large as in the troposphere, indicating a growth in wave energy density with altitude. That the log magnitude is approximately described by a Gaussian implies that the spectral magnitudes are approximately lognormally distributed.

Histograms of the spectral slope are shown in Figure 6. The mean slopes in the troposphere and the stratosphere are –2.5 and –2.4, respectively. These slopes are significantly smaller than the –3 slope predicted by theoretical models [e.g., *Weinstock*, 1990; *Gardner*, 1994; *Hines*, 1991, 1997a, b] and the slopes obtained by AV95 at most stations, particularly in the troposphere. It is interesting to note that in AV95, there seems to be a trend of decreasing spectral slope with increasing latitude, particularly in the stratosphere. The –2.4 slope we obtained at South Pole fits well

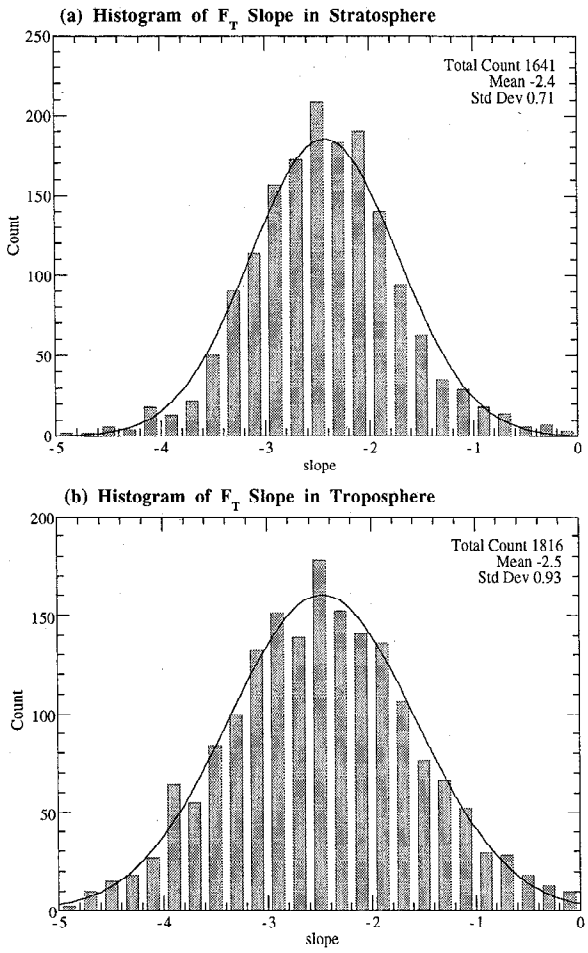

Figure 6. Histograms of the spectral slopes of temperature variations and their best fit Gaussian distribution in the (a) stratosphere and (b) troposphere.

with this trend, as illustrated by Figure 7. This trend may be associated with the latitudinal changes in the mix of wave sources in the troposphere or changes in background atmospheric structure in which the gravity waves propagate. Best fit Gaussian distribution curves are also plotted in Figure 6. The probability distribution of spectral slope is also approximately normal.

NVW97 have shown that there is a relation between spectral slope and spectral magnitude. Our South Pole data exhibit only minimal correlation between slope and spectral magnitude in either the troposphere or the stratosphere (not shown). The correlation coefficients in both regions are less than 0.2, implying that slope and magnitude are nearly independent.

6.4. Relation Between Troposphere and Stratosphere

If gravity waves generated in the troposphere propagate primarily into the lower stratosphere without breaking or saturation, there should be a significant correlation in the spectral properties of these two regions. This can be examined with Figure 8 which shows scatterplots of the spectral magnitudes and slopes in the stratosphere versus those in the troposphere. The correlation coefficient is 0.19 for the magnitude and 0.11 for the slope. NVW97 obtained correlation values of –0.13 for the magnitude and 0.01 for the slope. These correlation coefficients are all very small, suggesting that little coherence exists between waves in the troposphere and waves in the stratosphere. On the other hand, NVW97 found significant correlation in the wind spectrum and claimed that the low correlation in the temperature spectra was due to relatively large errors. In this study, we cannot obtain a reliable estimate of the correlation of the wind spectra due to the large uncertainty in the wind data at the shorter vertical scales. However, we are confident of the temperature spectra, since there is no significant noise floor in the temperature spectra in Plate 4. That the wave characteristics in the troposphere and stratosphere are uncorrelated suggests that a significant portion of the waves in the stratosphere may have different sources than those in the troposphere. This possibility is further examined in section 7.

6.5. Seasonal Variation

The 4-year continuous data set provides an excellent opportunity to examine the seasonal and interannual variations of gravity wave activity at South Pole. Harmonics are obtained for the time series of spectral magnitude and slope using a least squares fit for each independent harmonic. Fitting is performed in the log domain for spectral magnitude. The parameters of these harmonics

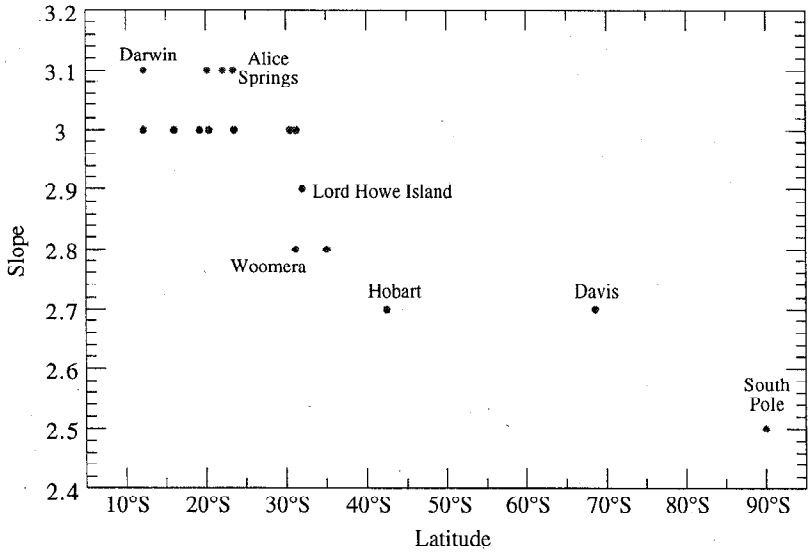

Figure 7. Latitudinal variation of spectral slope in the stratosphere. Data point at South Pole is obtained from this study. All other data points are based on AV95.

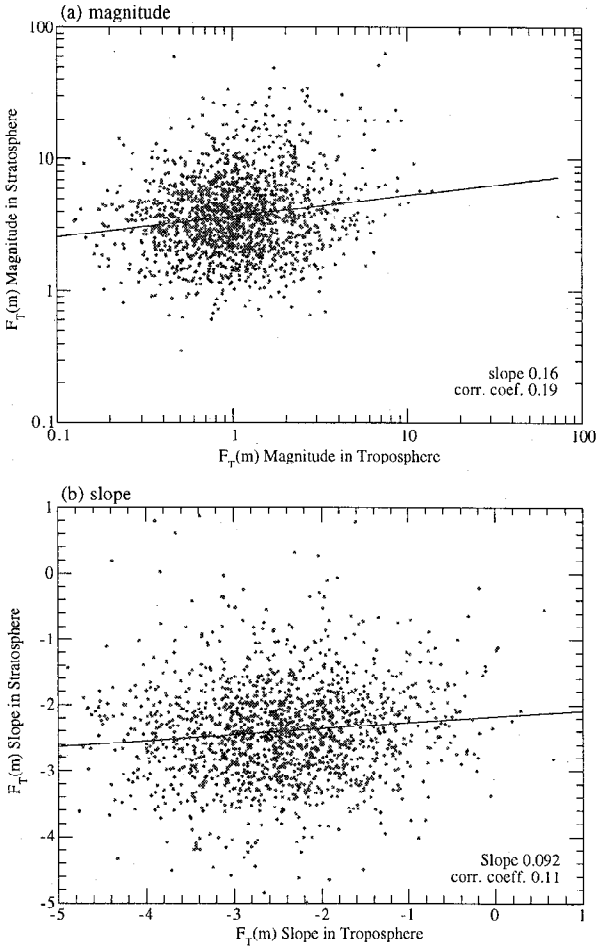

Figure 8. (a) Magnitude and (b) slope of temperature spectra in the stratosphere versus those in the troposphere.

are shown in Table 2 along with the 1-σ error estimates. For the amplitude of the harmonics, it can be seen that in the troposphere, only the slope with periods of 12, 8, and 6 months are statistically meaningful; in the stratosphere, only the 12-month period is statistically meaningful for both magnitude and slope. This indicates that the dominant component of the variation is in seasonal timescale. In Figure 9, the 4-year weekly-averaged spectral magnitude and slope are shown as gray curves. Overlaid on top of them (dark curves) are smoothed time series which include all harmonics with periods longer than or equal to four months. Figure 9 shows that large fluctuations exist in the spectral magnitudes and slopes for both the troposphere and the stratosphere. The smoothed curves are good representation of the seasonal variation. It is clear that both magnitudes and slopes have fairly large seasonal variations in the stratosphere. In the troposphere, only the slopes have a large variation. The spectral magnitude in the troposphere does not have much seasonal variation, even though there are still large weekly fluctuations. There are also noticeable year-to-year variations. For example, magnitudes in the stratosphere (Figure 9a) are large in October 1993 and 1995, but smaller in October 1994 and 1996. Slopes in the stratosphere (Figure 9b) are dominated by 4-month-period variation in the first 2 years, and then dominated by longer-period variations in the last 2 years.

To further illustrate the annual variation of the temperature spectra at South Pole, we show in Figure 10 the time series of the spectral magnitudes and slopes including only the 1-year, 6-month and 4-month period Fourier harmonics (see Table 2). These are the main components of the annual cycle. The spectral magnitude in the stratosphere reaches a maximum (minimum) in early November (late April). The maximum is over twice as large as the minimum. From Plate 1a, we can see that early November is the time when the stratosphere warms rapidly from above yet is still very cold below. This creates a more stable stratification favorable for gravity wave propagation. The spectral magnitude in the troposphere has very small annual variation, with maximum (minimum) around late March (early October). It is negatively correlated with the variation in the stratosphere with a correlation coefficient of –0.77.

The spectral slopes show similar seasonal variation in the stratosphere and troposphere. The cross-correlation coefficient is 0.52. In the stratosphere the absolute value of the slope is minimum in late April and maximum in February. In the troposphere the absolute value of the slope is largest during austral summer (December to January) and smallest during austral winter (August). These seasonal variations appear to be associated with the large differences of background atmospheric conditions, such as wind shear and static stability in different seasons.

The solid and open circles in Figure 10 show the weekly-averaged values in the troposphere and stratosphere, respectively. These circles have very large spread, indicating large interannual variations in addition to the annual variation.

7. Gravity Wave Propagation

7.1. Method

From the wind and the temperature perturbations, it is possible to estimate the dominant direction of gravity wave propagation and other important wave parameters. This information can help identify the gravity wave sources and provide quantitative information on the wave propagation characteristics. Our analysis method follows *Vincent and Fritts* [1987] and *Eckermann and Vincent* [1989]. A set of parameters describing a gravity wave can be constructed in analogy to the Stokes parameters for electromagnetic waves [*Vincent and Fritts*, 1987]:

$$I = \overline{u'^2} + \overline{v'^2},\ P = 2\overline{u'v'},\ D = \overline{u'^2} - \overline{v'^2},\ Q = 2\overline{u'v'_{+90}}, \quad (9)$$

where u' and v' are wind perturbations and the overbar represents a sample average over altitude. I is a measure of the total kinetic energy, P and D are measures of linear polarization, Q is a

Table 2. Parameters of the Fit Curves of Figure 8

Period,	$\mathrm{Log}_{10}\left(F_T(2\pi/400\ \mathrm{m})\right)$		Power-Law Slope	
months	A	ϕ (rad)	A	ϕ (rad)
		Troposphere		
∞	0.11±0.01	N.A.	-2.50±0.03	N.A.
48	0.02±0.02	0.22±0.93	0.03±0.04	0.53±1.63
24	0.01±0.02	2.98±3.12	0.06±0.04	2.88±0.73
12	0.02±0.02	3.03±0.74	0.18±0.04	0.05±0.22
8	0.03±0.02	-0.86±0.65	0.08±0.04	2.58±0.53
6	0.00±0.02	-0.44±4.74	0.07±0.04	-0.90±0.55
4	0.01±0.02	-2.50±1.40	0.03±0.04	2.22±1.14
		Stratosphere		
∞	0.62±0.02	N.A.	-2.43±0.03	N.A.
48	0.04±0.02	-1.29±0.55	0.08±0.04	0.63±0.48
24	0.04±0.02	-2.65±0.52	0.05±0.04	2.37±0.74
12	0.17±0.02	-1.08±0.11	0.15±0.04	-0.41±0.25
8	0.03±0.02	1.54±0.68	0.03±0.04	2.80±1.17
6	0.03±0.02	-0.62±0.54	0.09±0.04	0.88±0.42
4	0.04±0.02	2.29±0.44	0.13±0.03	2.37±0.26

Fits are the sum $\sum A\cos(\omega t - \phi)$. N.A., not available.

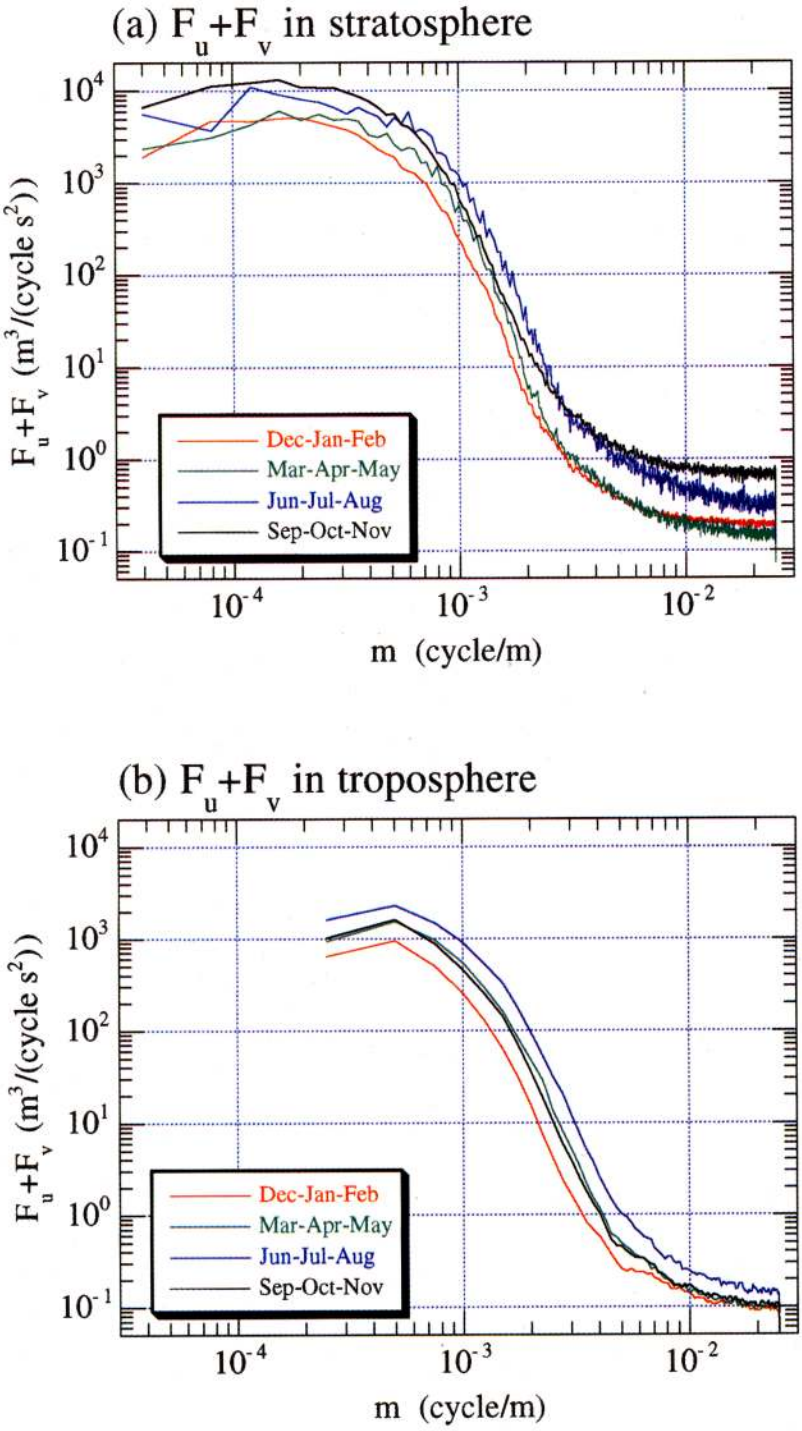

Plate 5. Seasonal mean wind spectra in the (a) stratosphere and (b) troposphere.

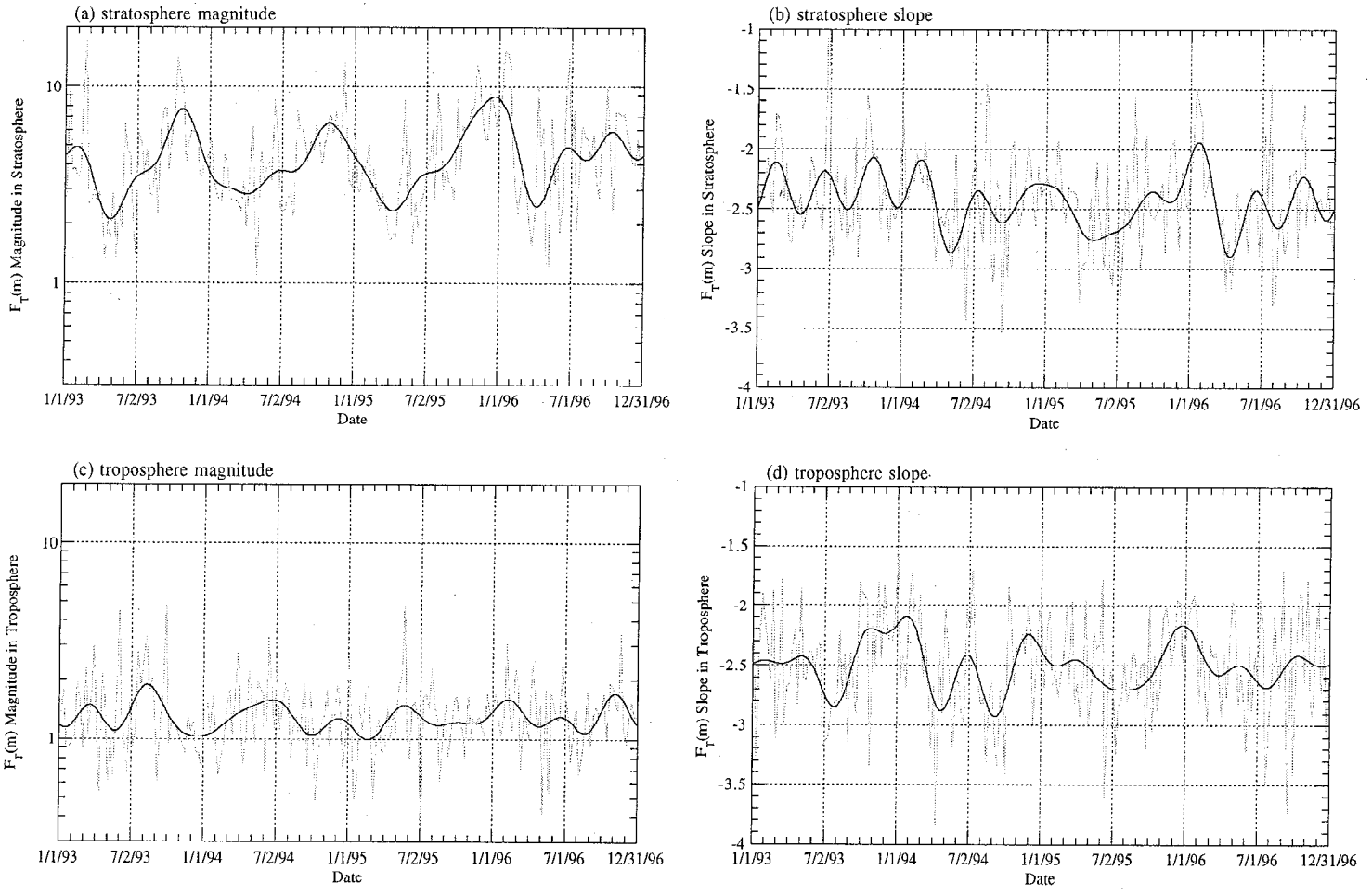

Figure 9. Variation of temperature spectra magnitude and slope in the troposphere and the stratosphere. Gray curves are weekly averaged values. Dark curves are the least squares fit of the first 12 harmonics (periods ≥ 4 months). The parameters of this fit are summarized in Table 2.

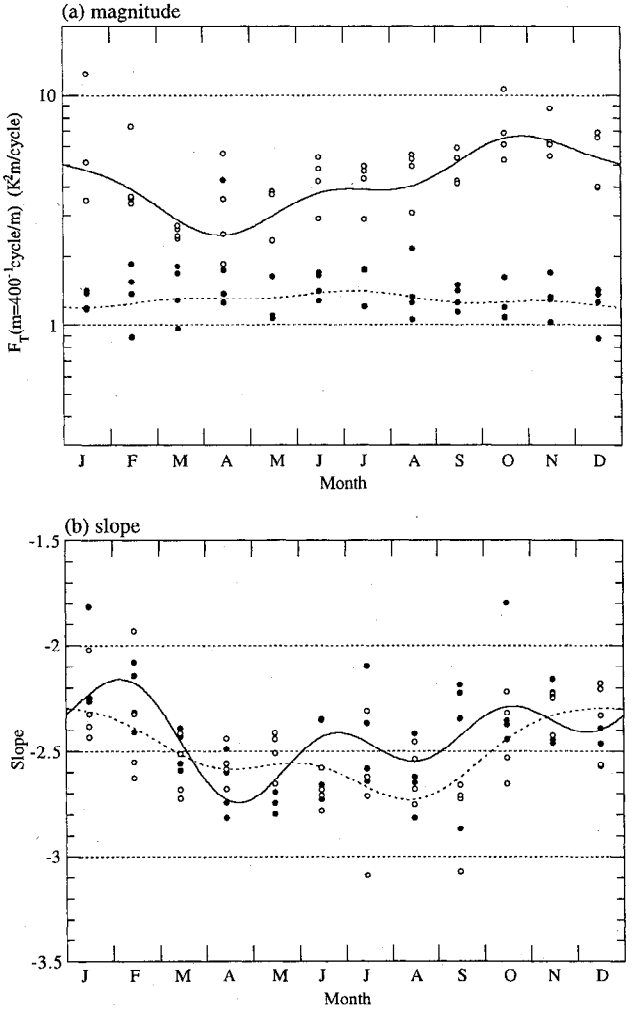

Figure 10. Four-year averaged seasonal variation of temperature spectral (a) magnitude and (b) slope.

measure of the circular polarization; and v'_{+90} is the Hilbert transform of v', which adds a 90° phase shift in the vertical profile. The polarization factor d is defined as

$$d = \left(P^2 + D^2 + Q^2\right)^{1/2} / I. \tag{10}$$

For a monochromatic wave, $d = 1$. For an isotropic distribution of waves with random phase and wavenumber, $d = 0$. The polarization factor is a statistical measure of the coherence of the wave field. From these parameters, we can estimate the dominant horizontal and vertical propagation directions.

Because of Coriolis force, the wind vector rotates with height. The trajectory of the wind vector forms an ellipse. The orientation of the major axis of this ellipse is given by

$$\tan 2\alpha = P/D, \tag{11}$$

where α is the angle measured anticlockwise from the x axis (grid east at South Pole). For gravity waves, the horizontal direction of propagation is along the major axis. Therefore α gives the direction of propagation with a 180° ambiguity. This ambiguity can be removed using information in the temperature perturbations. For a single gravity wave, the temperature perturbation is always in quadrature with the wind perturbation along the major axis. Let $U' = u'\cos\alpha + v'\sin\alpha$ be the wind in the direction of the major axis. The sign of $U'T'_{+90}$ then determines the direction of propagation, where T'_{+90} is the Hilbert transform of the temperature perturbation. Specifically, positive (negative) $U'T'_{+90}$ indicates that the direction of propagation is α ($\alpha \pm 180°$). In the presence of many waves, this method gives a statistical estimate of the dominant direction of horizontal propagation of the wave field.

For upward propagating gravity waves (downward phase propagation) in the southern hemisphere, the horizontal velocity vector rotates anticlockwise with increasing height, and clockwise for downward propagating waves. Since the Stokes parameter Q is a correlation between u' and v'_{+90}, it can be used to estimate the rotating direction of the wind vectors and thus infer the direction of vertical wave propagation. We can think of Q as the energy difference between the upward and downward propagating waves for each sounding profile. Positive (negative) Q indicates that most of the wave energy is propagating upward (downward).

7.2. Results

Histograms of the polarization factor are shown in Figure 11. The data show that the gravity waves are generally well polarized over the south pole, indicating that the majority of the time, there are a few dominant waves present in the balloon profiles instead of a mixture of many waves with nearly random distribution of propagation directions. The average polarization factors in the troposphere and stratosphere are comparable. The large number of soundings with the polarization factor near one suggests that

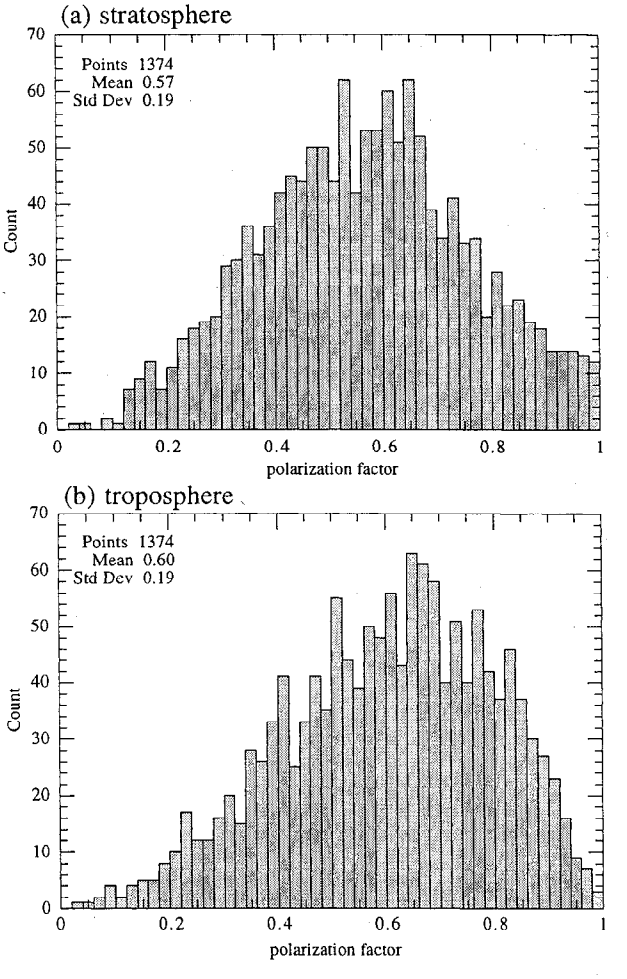

Figure 11. Histogram of polarization factor in the (a) stratosphere and (b) troposphere.

the perturbations are often quasi-monochromatic. This feature is similar to other observations such as in the work by *Vincent et al.* [1997]. It should be noted that sometime seemingly monochromatic features can be produced by the superposition of many waves [*Eckermann and Hocking,* 1989].

The histogram of the Stokes parameter Q is shown in Figure 12. In the troposphere the distribution is symmetric, which means that there are about equal number of soundings with dominant upward and downward propagation. In the stratosphere, the distribution is highly asymmetric, with about 80% of the soundings with dominant upward propagation. This suggests that in addition to the gravity waves generated in the lower troposphere (which contribute to the upward propagation in the troposphere and stratosphere), many waves are also generated in the upper troposphere or lower stratosphere (which contribute to the downward propagation in the troposphere and upward propagation in the stratosphere). The different wave sources in troposphere and stratosphere contributes to the low correlation between the spectral characteristics in these two regions as shown in section 6.4.

Following *Vincent et al.* [1997], the horizontal propagation directions are illustrated by plotting the "angular spectrum," which is obtained by binning the horizontal directions into 30° segments weighted by the total energy. The magnitude of each bin Φ_i is determined by

$$\Phi_i = \sum_{j=1}^{M_i} E_{i,j} \Big/ E_T, \quad i = 1, \ldots, 12, \tag{12}$$

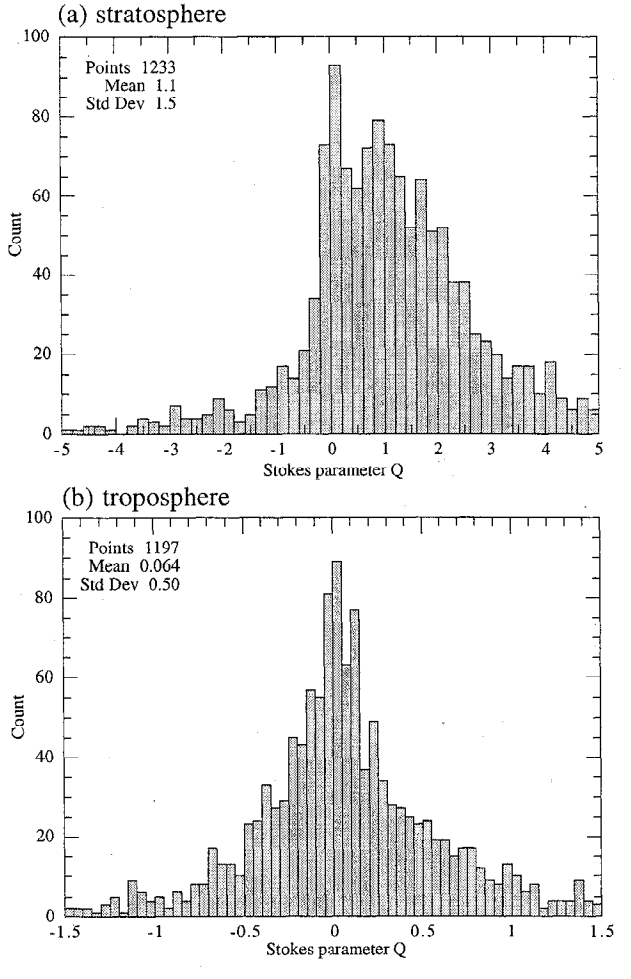

Figure 12. Histogram of Stokes parameter Q in the (a) stratosphere and (b) troposphere.

where $E_{i,j}$ is the wave energy for a single sounding and M_i is number of soundings in the ith bin, and

$$E_T = \sum_{i=1}^{12} \sum_{j=1}^{M_i} E_{i,j} \tag{13}$$

is the sum of $E_{i,j}$ for all 12 bins. The magnitude of Φ_i is a measure of the probability of gravity waves propagating within the direction of the ith bin. The binning is done for four seasons separately with all 4-year soundings as well as for the entire 4-year data. Since we found no significant seasonal variations of the horizontal propagation direction, only the 4-year average is shown in Figure 13. It is clear that there is no preferred direction with dominant energy in either the troposphere or the stratosphere. The lack of a dominant propagation direction can be expected because of the lack of strong anisotropic features in orography or other geographically fixed sources at South Pole.

Besides gravity wave sources, the mean background wind also affects the direction of wave propagation. To examine the characteristics of the background flow in which the gravity waves propagate, we plot the vertically-averaged mean horizontal wind with the same binning method, except use wind speed instead of energy for the weighting. Figure 14 shows the distribution of mean wind averaged over 4 years in the troposphere and the stratosphere. It is clear that the mean wind is generally toward grid-southeast in the troposphere and toward grid-northwest in the stratosphere. Because the orography in Antarctica is such that the elevation is high to the grid-northeast and low to grid-southwest of the south pole, the northwesterly mean wind in the troposphere is in agreement with geostrophic balance requirement. The katabatic low-altitude winds generally flow from elevated regions of the polar plateau to lower altitudes, under the additional influence of Coriolis accelerations. The nearly opposite direction of mean wind in the troposphere and stratosphere indicates persistent vertical wind shear. This could provide a mechanism for gravity wave generation. On average, the wind speed is less than 10 m/s in the stratosphere and less than 5 m/s in the troposphere. The mean wind influence on the wave propagation direction is therefore not significant.

We also examined the possible influence of the direction of solar radiation on the direction of wave propagation by separating the soundings near 0800 and near 2000UT in the austral summer. Again, we found no significant difference in the direction of propagation between these two times, which indicates that the solar azimuth angle has little influence on the direction of gravity wave propagation.

8. Stability

The presence of gravity waves changes the stability of the atmosphere. When the wave amplitude is large enough, instabilities may be generated, which lead to the breakdown of the wave. By computing how frequently waves reach instability, we can infer important information about how energy is exchanged between the wave and the mean background, how far a wave can propagate, and how valid the approximate linear wave theory is. In this section, we estimate the probability of instability generated by two mechanisms, namely convective and dynamic (shear) instabilities. They can be measured by the Brunt-Väisälä frequency and the Richardson number, respectively. These two parameters are defined as

$$N^2 = g \frac{\partial \ln \theta}{\partial z}, \tag{14}$$

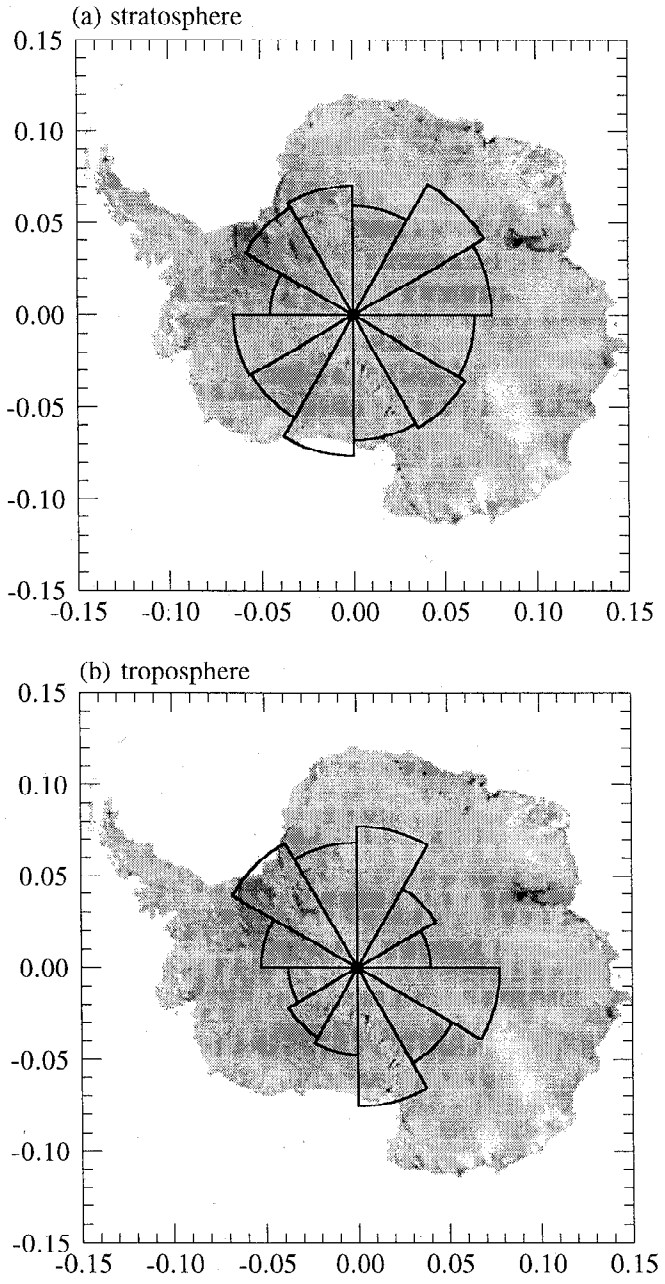

Figure 13. Probability distribution of horizontal wave propagation directions in the (a) stratosphere and (b) troposphere.

$$Ri = \frac{N^2}{\left(\partial u/\partial z\right)^2 + \left(\partial v/\partial z\right)^2}, \tag{15}$$

where θ is the potential temperature. Convective instability occurs when $N^2 < 0$ and $Ri < 0$, while dynamic instability occurs when $0 < Ri < 0.25$.

To examine the probability of instability due to these two mechanisms, we calculate N^2 and Ri for all soundings at all altitudes with the raw observed wind and temperature data, which include both the mean state and wave perturbations. To ensure uniform sampling through altitude, each sounding is first binned into 40-m intervals. For each sounding, the number of samples of N^2 and Ri is 100 in the troposphere and ranges from 400 to over 800 in the stratosphere, depending on the maximum altitude reached. The vertical derivatives in (14) and (15) are calculated by finite differencing. It is to be noted that since the high wavenumber components of the wind fluctuations are excessively filtered as shown in section 6.2, the actual Ri may be smaller. This means our results may underestimate the probability of dynamic instability.

The mean N^2 and Ri computed for each season are shown in Table 3. In Table 4 are the probabilities of convective and dynamic instability determined by integrating the appropriate regions of the N^2 and Ri distributions. The convective instability probability is generally small, averaging 2.6% in the troposphere and 0.7% in the stratosphere. The larger instability probability in the troposphere is a consequence of the smaller mean value for N^2. Due to the relatively warm boundary layer, in the tropo-

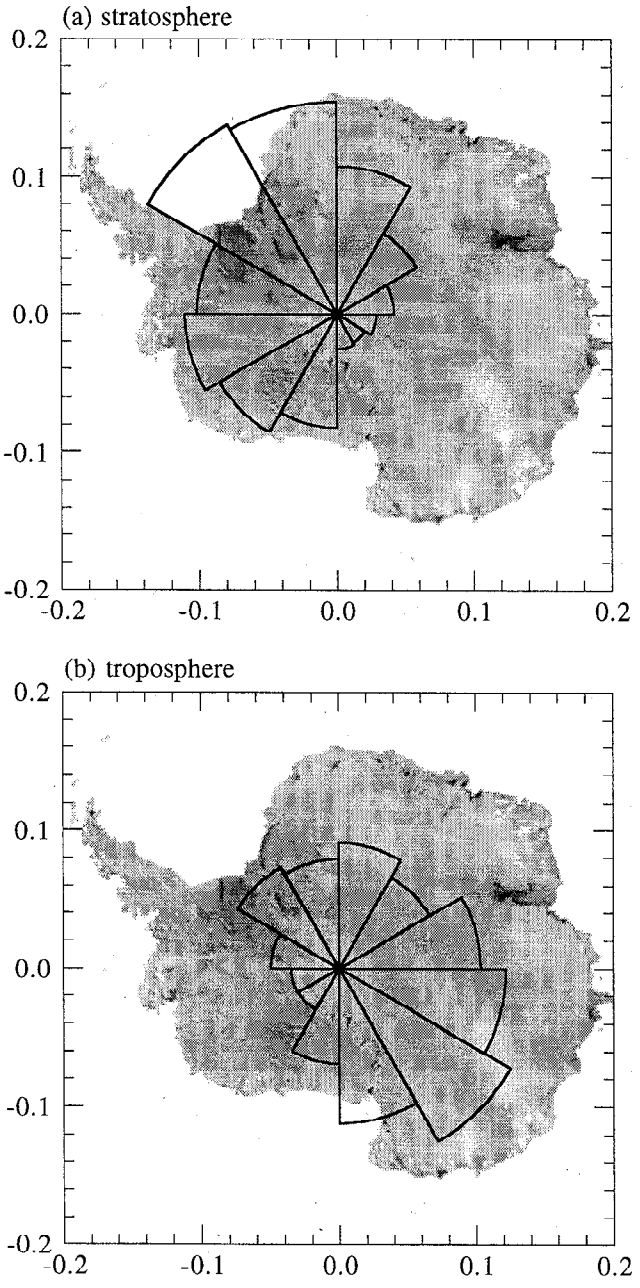

Figure 14. Probability distribution of normalized mean horizontal wind in the (a) stratosphere and (b) troposphere.

sphere the mean N^2 is $1.6\times10^{-4}s^{-2}$ (mean buoyancy period 8.2 min) compared to $4.5\times10^{-4}s^{-2}$ (mean buoyancy period 4.9 min) in the stratosphere. Although the distributions are not shown, the spread of the N^2 distribution is much larger in the stratosphere than in the troposphere, partly because wave amplitudes generally increase with height and partly because the mean temperature structure changes more dramatically in the stratosphere than in the troposphere.

As Table 4 shows, the dynamic instability has a higher probability than convective instability, averaging 11.1% in the troposphere and 4.7% in the stratosphere. The probability of instability is also significantly larger in the troposphere than in the stratosphere, associated with the difference in the mean values of N^2 in these two regions. Overall, the total probability of instability (convective plus dynamic) is 13.7% in the troposphere and 5.4% in the stratosphere.

There are seasonal variations of mean N^2 and convective instability, particularly in the stratosphere. The mean N^2 is largest in SON due to the warming in the middle stratosphere. The probability of convective instabilities in the stratosphere is relatively high in DJF and SON (1.3% and 1.2%, respectively) and low in MAM and JJA (0.18% and 0.25%, respectively). In the troposphere the mean N^2 are much smaller than in the stratosphere

Table 3. Mean N^2 ($10^{-4}s^{-2}$) and *Ri*

	Troposphere		*Stratosphere*	
	N^2	*Ri*	N^2	*Ri*
DJF	1.74	7.74	4.39	12.8
MAM	1.82	5.80	4.16	10.4
JJA	1.52	4.04	4.38	7.32
SON	1.46	5.33	5.04	8.74

Table 4. Probability of Instabilities

	$P(N^2<0)$	$P(0<Ri<0.25)$	$P(Ri<0.25)$
		Troposphere	
DJF	2.96	4.35	7.31
MAM	1.55	11.5	13.1
JJA	2.43	19.0	21.4
SON	3.66	9.56	13.2
		Stratosphere	
DJF	1.27	1.20	2.47
MAM	0.18	3.77	3.95
JJA	0.25	9.42	9.67
SON	1.22	4.27	5.49

Values are in percent.

because of the relatively warm boundary layer, and do not vary much through different seasons. The probability of convective instability in the troposphere is larger in DJF and SON (3.0% and 3.7%, respectively) than in MAM and JJA (1.5% and 2.4%, respectively). The relatively large probability of convective instability in both troposphere and stratosphere during austral spring and summer is related to relatively stronger wave activity.

There are also strong seasonal variation of Ri and the probability of dynamic instability. Comparing Tables 2 and 3, one can see that the variation of dynamic instability is just the opposite to the variation of mean Ri. Whenever Ri is large (weak wind shear), dynamic instability is less likely to occur, and vice versa. In both the troposphere and stratosphere, the dynamic instability is most likely to occur during austral winter (JJA) and least likely during austral summer (DJF). This seasonal variation is just the opposite to the variation of convective instability. Therefore wave breaking due to dynamic (convective) instability is more (less) likely during austral winter than during austral summer.

The total probability of instability are obtained by adding the percentages in columns two and three of Table 4. Because of the dominance of dynamic instability, the seasonal variation of total instability follows that of the dynamic instability. The largest instability probability of 21.4% is in the troposphere in austral winter; the smallest of 2.5% is in the stratosphere in austral summer.

9. Discussion and Summary

In this study, we analyzed the gravity wave characteristics at South Pole based on a 4-year data set from 1993 to 1996 obtained from over 2000 balloon soundings. Because of its special geographic location, South Pole is a unique place to study gravity waves. The rich 4-year data set enables us to study not only the gravity wave characteristics in individual soundings, but also the seasonal variation of these characteristics.

The background environment in which gravity waves are generated and through which they propagate is easily segmented into two primary seasons. In austral summer (DJF) the temperature structure follows the canonical form generally assumed for the lower atmosphere. Background temperatures decrease from the surface to about the tropopause. The mean temperature has a strong vertical gradient in the austral spring, caused by heating from the middle or upper stratosphere. Associated with the temperature gradient, the static stability also increases in the mid-stratosphere in early spring. The increased static stability allows more waves to propagate upward and results in strong wave activity in the stratosphere. Some of the strongest wave activity also occurs in the mid-winter stratosphere, where total energy densities can reach above 10 J/kg.

The characteristics of vertical wavenumber spectra in the wave field at South Pole are, in general, similar to those obtained at other locations around the globe. Our wave variance results follow the latitudinal trends suggested by AV95, who analyzed the gravity waves in multiple stations covering a broad latitudinal band in the southern hemisphere and showed that total wave energy decreases with increasing latitude. The main difference between our results and those of AV95 and others is that the spectral slope in the power law region over South Pole is smaller than those obtained from lower-latitude stations. Examination of the literature suggests that a general trend may exist, with higher latitudes experiencing shallower spectral slopes.

We see no correlation between the tropospheric and stratospheric spectral characteristics. We have also found strong systematic variations of both spectral slopes and spectral magnitudes on various timescales. In addition to the chaotic daily fluctuations, there are strong seasonal variations particularly in the stratosphere. These variations are associated with the seasonal variation of background atmospheric conditions.

We have estimated the direction of gravity wave propagation with a method similar to that of *Vincent and Fritts* [1987] and *Vincent et al.* [1997]. As expected, the horizontal propagation does not have a preferred direction, due to the relatively featureless topography at South Pole and lack of an anisotropic distribution of gravity wave sources. In the vertical direction, the distribution of Stokes parameter Q shows that in the stratosphere 80% of the soundings are dominated by upward propagating waves, while in the troposphere the number of soundings dominated by downward and upward propagation are about the same. This suggests the existence of some gravity wave sources in the upper troposphere or lower stratosphere, possibility due to instabilities generated by strong wind shear.

The buoyancy frequency squared N^2 and the Richardson number Ri for each individual sounding at different altitudes are calculated to determine the stability properties of the atmosphere in the presence of waves. Our calculations show that the instabilities are more likely to occur in the troposphere than in the stratosphere because of the smaller buoyancy frequency in the troposphere associated with the warm boundary layer. Dynamic instability is more probable than the convective instability due to the presence of strong vertical shear in the mean wind. The instability probabilities also vary with season. Convective instabilities are more probable in austral summer, while the dynamic instabilities are more probable in austral winter.

Our results in this study suggest that the current gravity wave theories are not adequate in describing the observed wave spectrum. Combined with the study of AV95, it is clear that the gravity wave characteristics vary with latitude and are influenced by various atmospheric background condition. Incorporating these effects into gravity wave theories and parameterization schemes is therefore very important.

Acknowledgments. The authors would like to thank Dr. Lamont Poole of NASA Langley for supplying several high-altitude balloons which were used for collecting a number of wintertime data. This research was supported in part by NSF grants NSF-OPP92-19898DPP and NSF-OPP96-16664 and by NASA grant 94-NASA-P/G-1718.

References

Allen, S. J., and R. A. Vincent, Gravity wave activity in the lower atmosphere: Seasonal and latitudinal variations, *J. Geophys. Res., 100*, 1327-1350, 1995.

de la Torre, A., P. Alexander, and A. Giraldez, High-resolution temperature profiles measured with stratosphere balloons near the Andes Mountains, *Geophys. Res. Lett., 24,* 1079-1082, 1997.

Dewan, E. M., and R. E. Good, Saturation and the "universal" spectrum for vertical profiles of horizontal scalar winds in the atmosphere, *J. Geophys. Res., 91,* 2742-2748, 1986.

Eckermann, S. D., Effect of background winds on vertical wavenumber spectra of atmospheric gravity waves, *J. Geophys. Res., 100,* 14,097-14,112, 1995.

Eckermann, S. D., and W. K. Hocking, Effect of superposition on measurement of atmospheric gravity waves: A cautionary note and some reinterpretations, *J. Geophys. Res., 94,* 6333-6339, 1989.

Eckermann, S. D., and R. A. Vincent, Falling sphere observations of anisotropic gravity wave motions in the upper stratosphere over Australia, *Pure Appl. Geophys., 130,* 509-532, 1989.

Fritts, D. C., and W. Lu, Spectral estimates of gravity wave energy and momentum fluxes, II, Parameterization of wave forcing and variability, *J. Atmos. Sci., 50,* 3695-3713, 1993.

Fritts, D. C., and T. E. VanZandt, Spectral estimates of gravity wave energy and momentum fluxes, I, Energy dissipation, acceleration, and constraints, *J. Atmos. Sci., 50,* 3685-3694, 1993.

Gardner, C. S., Diffusive filtering theory of gravity wave spectra in the atmosphere, *J. Geophys. Res., 99,* 20,601-20,622, 1994.

Gardner, C. S. and N. F. Gardner, Measurement distortion in aircraft, space shuttle, and balloon observations of atmospheric density and temperature perturbation spectra, *J. Geophys. Res., 98,* 1023-1033, 1993.

Hamilton, K., Comprehensive meteorological modeling of the middle atmosphere: a tutorial review, *J. Atmos. Terr. Phys., 58,* 1591-1627, 1996.

Hines, C. O., The saturation of gravity waves in the middle atmosphere, II, Development of Doppler-spread theory, *J. Atmos. Sci., 48,* 1360-1379, 1991.

Hines, C. O., Doppler-spread parameterization of gravity-wave momentum deposition in the middle atmosphere, 1, Basic formulation, *J. Atmos. Sol.-Terr. Phys., 59,* 371-386, 1997a.

Hines, C. O., Doppler-spread parameterization of gravity-wave momentum deposition in the middle atmosphere, 2, Broad and quasi monochromatic spectra, and implementation, *J. Atmos. Solar-Terr. Phys., 59,* 387-400, 1997b.

Hitchman, M. H., J. C. Gille, C. D. Rodgers, and G. Brasseur, The separated polar winter stratopause: A gravity wave driven climatological feature, *J. Atmos. Sci., 46,* 410-422, 1989.

Holton, J. R., *An Introduction to Dynamic Meteorology, 3rd ed.*, Academic, San Diego, Calif., 1992.

Lalas, D. P., and F. Einaudi, Tropospheric gravity waves: Their detection by and influence on rawinsonde balloon data, *Q. J. R. Meteorol. Soc., 106,* 885-864, 1980.

Lindzen, R. S., Turbulence and stress owing to gravity wave and tidal breakdown, *J. Geophys. Res., 86,* 9707-9714, 1981.

Medvedev, A. S., and G. P. Klaassen, Vertical evolution of gravity wave spectra and the parameterization of associated wave drag, *J. Geophys. Res., 100,* 25,841-25,853, 1995.

Nastrom, G. D., T. E. VanZandt, and J. M. Warnock, Vertical wavenumber spectra of wind and temperature from high-resolution balloon soundings over Illinois, *J. Geophys. Res., 102,* 6685-6701, 1997

Sidi, C., J. Lefrere, F. Dalaudier, and J. Barat, An improved atmospheric buoyancy wave spectrum model, *J. Geophys. Res., 93,* 774-790, 1988.

VanZandt, T. E., and D. C. Fritts, A theory of enhanced saturation of the gravity wave spectrum due to increase in atmospheric stability, *Pure Appl. Geophys., 130,* 399-420, 1989.

Vincent, R. A., and D. C. Fritts, A climatology of gravity wave motions in the mesopause region at Adelaide, Australia, *J. Atmos. Sci., 44,* 784-760, 1987.

Vincent, R. A., S. J. Allen, and S. D. Eckermann, Gravity-wave parameters in the lower stratosphere, *NATO Advanced Research Workshop, Gravity Wave Processes - Their Parameterization in Global Climate Models*, edited by K. Hamilton, *ASI Ser. I 50,* pp. 7-25, Springer-Verlag, New York, 1997.

Weinstock, J., Saturated and unsaturated spectra of gravity waves and scale-dependent diffusion, *J. Atmos. Sci., 47,* 2211-2225, 1990.

C. S. Gardner, A. Z. Liu, G. C. Papen, M. Pfenninger, Department of Electrical and Computer Engineering, University of Illinois at Urbana-Champaign, 308 CSRL, 1308 West Main Street, Urbana, IL 61801. (email: cgardner@uiuc.edu; liuzr@uiuc.edu; g-papen@uiuc.edu; pfennin@ripley.ece.uiuc.edu.)

(Received July 21, 1998; revised July 21, 1998; accepted August 10, 1998)